Full-Envelope Aero-Propulsive Model Identification for Lift+Cruise Aircraft Using Computational Experiments

Benjamin M. Simmons,[*] Pieter G. Buning,[†] and Patrick C. Murphy[‡]
NASA Langley Research Center, Hampton, VA, 23681

This paper describes a process utilizing computational fluid dynamics experiments to develop a reduced-order, integrated propulsion-airframe aerodynamic model for a lift+cruise electric vertical takeoff and landing (eVTOL) reference aircraft concept. eVTOL configurations exhibit aerodynamic characteristics of both fixed-wing and rotary-wing aircraft as well as complex phenomena, such as propulsion-airframe interactions. Consequently, conventional aircraft aerodynamic modeling strategies require modification when applied to these unique aircraft. A novel aero-propulsive modeling approach using design of experiments techniques and computational fluid dynamics simulations is postulated for modeling a lift+cruise aircraft configuration. Aero-propulsive models are developed throughout the operational flight envelope to enable continuous flight dynamics simulations from hover through forward flight. The model adequacy is assessed using validation data acquired separately from data used to identify the model and indicates that the models have sufficient predictive capability. Research findings are presented with a discussion of unique lift+cruise aircraft aerodynamic characteristics and practical strategies to inform future aero-propulsive modeling and simulation efforts for eVTOL aircraft.

Nomenclature

b = wingspan, ft
C_x, C_y, C_z = dimensionless body-axis force coefficients
C_l, C_m, C_n = dimensionless body-axis moment coefficients
$\bar{c}$ = mean aerodynamic chord, ft
D = rotor and propeller diameter, ft
e^* = normalized residual
J = advance ratio
L, M, N = body-axis aero-propulsive moments, ft-lbf
n = rotor and propeller rotational speed, revolutions/s
p, q, r = body-axis angular velocity components, rad/s
$\bar{q}$ = freestream dynamic pressure, lbf/ft^2
S = wing area, ft^2
u, v, w = body-axis translational velocity components, ft/s
V = freestream airspeed, ft/s
X, Y, Z = body-axis aero-propulsive forces, lbf
α = angle of attack, rad or deg
β = angle of sideslip, rad or deg
ρ = air density, slug/ft^3

Superscripts
^{T} = transpose
$\dot{\ }$ = time derivative

---

[*] Research Engineer, Flight Dynamics Branch, MS 308, AIAA Member.

[†] Senior Research Scientist, Computational AeroSciences Branch, MS 128, AIAA Associate Fellow.

[‡] Senior Research Engineer, Dynamic Systems and Control Branch, MS 308, AIAA Associate Fellow.

I. Introduction

Electric vertical takeoff and landing (eVTOL) aircraft enabling future Urban Air Mobility (UAM) transportation missions are gaining interest in the aerospace industry. UAM vehicles require precise hover and efficient cruise capabilities as well as the ability to safely transition between flight regimes. eVTOL aircraft are a hybrid between traditional fixed-wing and rotary-wing aircraft utilizing certain attributes of each type of vehicle. Fixed-wing aircraft contribute longer endurance, better efficiency, and the ability to operate at high speeds. Rotorcraft have the ability to takeoff and land vertically, hover, and precisely maneuver in confined areas. eVTOL aircraft also uniquely utilize distributed electric propulsion technology, which has broadened the traditional aeronautical vehicle design space and resulted in numerous novel vehicle designs [1, 2].

While eVTOL vehicles' hybrid configurations are convenient from an operational standpoint [3], there are many research areas to be addressed prior to introduction of operational eVTOL vehicles for a UAM mission [4]. eVTOL vehicle technical challenges include airworthiness certification, air traffic management, pilot-operator interface, handling qualities, simplified vehicle operations, contingency management, vehicle autonomy, and flight controls strategies. One important enabling tool for many eVTOL research efforts is an accurate vehicle flight dynamics model, but the current modeling state-of-the-art for eVTOL vehicles heavily relies on low-fidelity conceptual design tools, such as NDARC [5] and VSPAero [6]. Consequently, development of high-fidelity aerodynamic models for eVTOL aircraft is a crucial need, however, eVTOL-specific aerodynamic model strategies are largely unexplored. Thus, development of high-fidelity aerodynamic models for eVTOL configurations is a new, critical area of research where novel aerodynamic modeling strategies are needed to appropriately represent pertinent aerodynamic phenomena specific to these unique vehicles.

eVTOL aircraft aerodynamic modeling is a challenge due to several vehicle attributes which hamper model development. These features include many control surfaces and propulsors, propulsion-airframe interactions, propulsor-propulsor interactions, high-incidence angle propulsor aerodynamics, vehicle instability, rapidly changing aerodynamics through transition, and large flight envelopes that need to be characterized by a global aerodynamic model. Since propulsion aerodynamics, airframe aerodynamics, and propulsion-airframe interactional aerodynamics are generally highly coupled for eVTOL aircraft, their aerodynamic models represent a combination of propulsion and airframe aerodynamics characteristics. For this reason, eVTOL aircraft aerodynamic models can also be referred to as aero-propulsive models. Most past eVTOL modeling work has used analytical and semi-empirical models to develop vehicle models for research applications; however, these are low-fidelity methods which drastically simplify highly complex aerodynamics. Ref. [7] highlights many of these efforts for a variety of different hybrid vehicles including tilt-wing, tilt-rotor, tail sitters, and dual-propulsion system configurations. The subset of eVTOL aircraft of interest in this work are dual-propulsion system vehicles where different propulsors are used for vertical and forward flight. This vehicle design is currently being referred to in literature as the lift+cruise configuration type [2].

Two predecessor aircraft to the vehicle studied in this work are subscale, tilt-wing, distributed electric propulsion, vertical takeoff and landing aircraft called the GL-10 [8] and LA-8 [9]. Several different scaled variants of the GL-10 and LA-8 vehicles were developed and tested to enable research in areas such as aerodynamic modeling [10–15], flight controls [16, 17], and flight testing [18, 19]. The complexity associated with these aircraft inspired an ongoing effort to develop a process to efficiently develop aerodynamic models for arbitrarily complex aerospace vehicles, referred to as Rapid Aero Modeling or RAM [20–22]. The RAM process utilizes design of experiments (DOE) theory [23] and a unique sequential modeling algorithm to develop aerodynamic models meeting a user-defined desired level of fidelity. DOE in this context also includes the field of response surface methodology (RSM). Model development strategies and lessons learned from these previous eVTOL aircraft studies, as well as the RAM process, informed the development of the aero-propulsive models presented in this work.

This work builds on previous eVTOL aircraft modeling research to develop a full-envelope, high-fidelity aero-propulsive model for the NASA Lift+Cruise aircraft concept [2]. Computational fluid dynamics (CFD) simulations are treated as an experimental data source, similar to static wind tunnel testing, to identify reduced-order response surface models sufficient for flight dynamics simulations. Consequently, the following discussion focuses on methods used to develop mathematical models from experimentally-derived data, termed aircraft system identification [24]. eVTOL vehicles exhibit aerodynamic characteristics similar to both fixed-wing and rotary-wing aircraft, but system identification approaches used for either type of vehicle type do not independently translate to modeling eVTOL vehicles [13]. This manuscript seeks to provide a thorough development and assessment of a new computational strategy for eVTOL aircraft modeling that can be applied prior to development of a physical vehicle.

The paper is organized as follows: Section II presents pertinent background information informing modeling strategies and introduces the experimental aircraft. Section III provides a synopsis of the RAM algorithm used for model development with Sec. IV providing more details on the methods used for model identification. The CFD data gathering effort is described in Sec. V. Postulation of lift+cruise vehicle-specific aero-propulsive modeling strategies are described in Sec. VI followed by sample modeling results presented in Sec. VII. Section VIII highlights flight dynamics simulation considerations and overall conclusions are summarized in Sec. IX.

II. Background

This section presents an overview of experimental fixed-wing and rotary-wing aircraft modeling techniques, which helps guide the development of the lift+cruise vehicle modeling approach described in the remainder of the paper. The section concludes with a description of the conceptual NASA Lift+Cruise aircraft.

A. Fixed-Wing and Rotary-Wing System Identification Approaches

Fixed-wing aircraft system identification techniques are well-developed for standard problems and have been applied successfully to numerous aircraft configurations [25, 26]. Aerodynamic modeling for fixed-wing aircraft is conventionally performed by developing data tables or functional representations of dimensionless aerodynamic force and moment coefficients as a function of aircraft states and controls. For subsonic aircraft, the dimensionless aerodynamic force and moment coefficients are conventionally expressed as a function of angle of attack α, angle of sideslip β, dimensionless angular rates $\hat{p}$, $\hat{q}$, $\hat{r}$, and control surface deflections, such as elevator δ_e, aileron δ_a, and rudder δ_r positions. The dimensionless forces and moments are termed response variables, or dependent variables; the airflow angles, angular rates, and control surface deflections are termed the explanatory variables. Models may be developed using computational methods, wind tunnel testing, or flight testing. The dimensionless force and moment coefficients in the aircraft body-axes are defined as

$$C_x = \frac{X}{\bar{q}S},\ C_y = \frac{Y}{\bar{q}S},\ C_z = \frac{Z}{\bar{q}S},\ C_l = \frac{L}{\bar{q}Sb},\ C_m = \frac{M}{\bar{q}S\bar{c}},\ C_n = \frac{N}{\bar{q}Sb} \tag{1}$$

where $\bar{q} = \frac{1}{2}\rho V^2$ is the freestream dynamic pressure. The forces are also commonly expressed in the stability-axes for modeling where lift coefficient C_L and drag coefficient C_D replace C_x and C_z.

Rotorcraft system identification follows different conventions from fixed-wing modeling, but is also well defined in the literature for helicopters and tilt-rotor variants [27]. Contrary to fixed-wing aircraft system identification, rotorcraft models generally rely more heavily on computational data or flight test data because wind tunnel testing is precluded by difficulties in scaling subscale rotary-wing vehicles and facility limitations [28]. Body-axis force and moment parameters are also generally estimated in their dimensional form due to the differences in scaling between rotor and fuselage aerodynamics. Stability-axes and wind-axes become undefined in hover, so modeling is generally only performed in the body-axes for rotorcraft. Rotorcraft system identification efforts most often develop linear models at a reference flight condition. These point models are only valid near the flight condition where they are identified and assume that complex rotorcraft aerodynamics can be represented in coupled, linear differential equations. The explanatory variables used for estimation are generally body-axis velocity components u, v, w, angular rates p, q, r, pilot control inputs, and rotor states, such as flapping, lead-lag, inflow, coning, engine dynamics, etc., depending on the design of the vehicle and the desired bandwidth of the developed model. Formulation in terms of body-axis velocity components, as opposed to airflow angles α and β, allows the state variables to be defined in hover and reflects the fact that fuselage angle of attack and angle of sideslip are less physically meaningful for describing rotorcraft aerodynamics. Models are commonly expressed in the form of a transfer function or state-space model with added time delay parameters to account for unmodeled higher-order dynamics [27].

Multirotor system identification has become a recent area of research interest with the growing availability and capabilities of electrically-powered unmanned aerial vehicles (e.g., see Refs. [29–32]). Multirotor modeling methodologies generally follow closely to rotorcraft system identification techniques, with the exception that certain rotor-specific states become less significant because the rotors generally have a smaller diameter, higher rigidity, and do not use cyclic pitch controls. Airframe-propulsion interactions can account for a significant portion of multirotor aerodynamic forces and moments [33], but are often ignored or lumped into quasi-steady, linear stability derivatives. The aerodynamic characteristics of lift+cruise aircraft configurations are generally a hybrid between multirotor and fixed-wing aircraft, depending on the operational flight mode.

B. Aircraft

The modeling approach presented in this paper for lift+cruise aircraft is described in the context of a recent NASA reference vehicle configuration introduced in Ref. [2]. This vehicle concept is referred to simply as "Lift+Cruise," where capitalization is used to distinguish from the generic "lift+cruise" configuration type. The purpose of the reference aircraft is to allow development of UAM enabling technologies, while also being impartial to prominent designs in industry.

The Lift+Cruise, pictured in Fig. 1, is a full-scale, vertical takeoff and landing, distributed propulsion aircraft concept with eight fixed-pitch lifting rotors and one variable-pitch, rear-mounted pusher propeller. The lifting rotors are intended to be used sparingly for takeoff, landing, and low-speed transition due to their high energy consumption. In high-speed cruise flight, the aircraft is only propelled by the pusher propeller and the two-bladed lifting rotors are aligned with oncoming airflow to minimize drag.

Fig. 1 Schematic of the NASA Lift+Cruise reference vehicle concept.

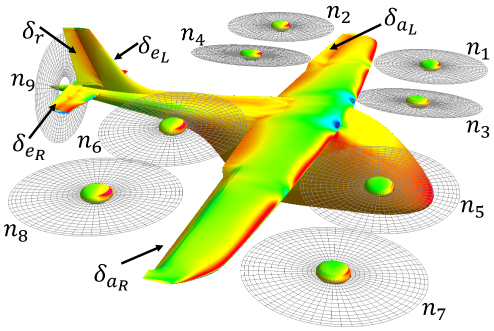

Fig. 2 Lift+Cruise propulsor and control surface definitions.

The conceptual Lift+Cruise variant studied for this research effort includes 14 total available control effectors including the nine aforementioned propulsors, two aileron surfaces, two elevator surfaces, and a rudder. A diagram of the propulsors and control surface definitions is shown in Fig. 2. The control surface deflections are denoted δ_{a_L} for left aileron, δ_{a_R} for right aileron, δ_{e_L} for left elevator, δ_{e_R} for right elevator, and δ_r for rudder. Aileron and elevator deflections are defined positive trailing edge downward and rudder deflection is defined positive trailing edge left. The lifting rotor rotational speeds are denoted n_1, n_2, ..., n_8. Rotors 2, 3, 6, and 7 rotate clockwise and rotors 1, 4, 5, and 8 rotate counterclockwise, as viewed from the top. The pusher propeller rotational speed is denoted n_9, and rotates clockwise as viewed from the rear.

III. RAM Algorithm

The Rapid Aero Modeling (RAM) algorithm is an efficient, statistically rigorous aircraft testing and model development approach that has been applied to both wind tunnel testing [21] and computational experiments [22]. RAM utilizes DOE and system identification theory to execute a unique, automated modeling process that continuously informs the user of modeling progress and, if desired, allows user intervention at certain stages. The RAM algorithm has been implemented into software as a collection of MATLAB scripts that has been used to develop aerodynamic models for several different aircraft. A flowchart illustrating the RAM process is shown in Fig. 3.

The RAM algorithm is initiated by providing information specific to the particular aircraft modeling effort including the explanatory variables, response variables, and a desired prediction error threshold. The algorithm then generates test matrices from a library of DOE test blocks. For each different number of experimental test factors, a series of five DOE test blocks are available to acquire the data necessary to identify increasingly complex aerodynamic models. Original block design was accomplished with the aid of Design-Expert®, a commercially available statistical software package.[*] The blocks are as follows: (1) face-centered design (FCD), (2) nested FCD [34], (3) I-optimal design for quadratic models, (4) I-optimal design for up to cubic models, and (5) I-optimal design used as validation data. Blocks (1) and (2) are each minimum run resolution V, face-centered, central composite designs. Minimum run resolution V fractional factorial designs contain the minimum number of test points to support estimation of linear and two-factor

---

[*] Information available online at https://www.statease.com/software/design-expert/ [accessed May 2021]

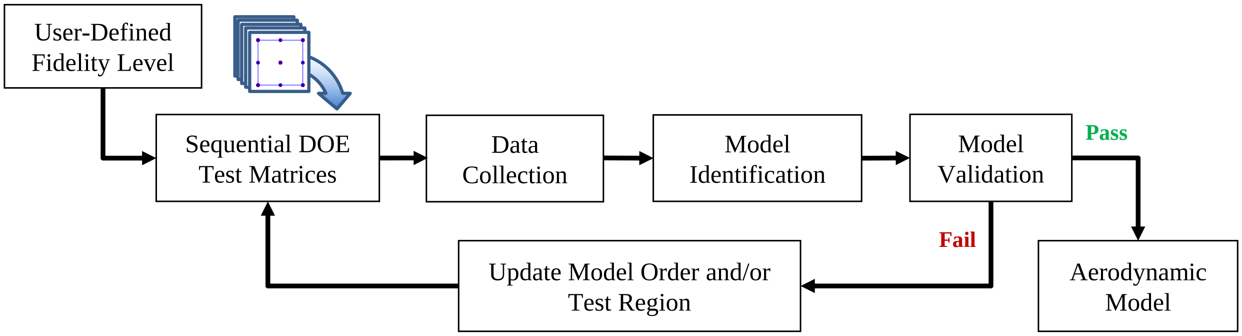

Fig. 3 RAM process flowchart.

interaction model terms. The nested FCD [34] augments the conventional FCD to provide greater data density within the factor space and allows estimation of pure cubic model terms. The subsequent I-optimal blocks are designed to minimize the integrated prediction variance over the range of factors, which reduces prediction error for the identified models [23]. Each I-optimal design augments the designs from previous blocks to sequentially improve the model and avoid duplicating previously tested combinations of factor settings. Blocks (3) and (4) are I-optimal designs which include the number of points required to fit a model for the specified complexity if the blocks were designed independently. The Block (5) I-optimal design contains 75 additional validation test points, which has been found to provide a good estimate of prediction error while remaining a modest number of test points. Figure 4 shows a two-dimensional slice of an experiment with 17 test factors; Fig. 4a shows Blocks 1-2 and Fig. 4b shows Blocks 3-5. Although “Coded Variable 1” and “Coded Variable 2” are shown in the figure, similar plots would be obtained for other test variables and the variables would be converted into engineering units before executing testing.

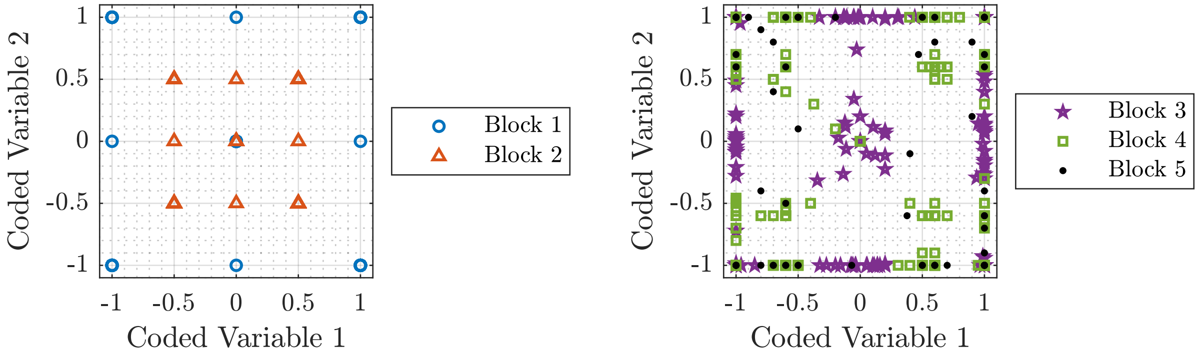

(a) Blocks 1 and 2 (FCD and nested FCD designs) **(b) Blocks 3, 4, and 5 (I-optimal and validation designs)**

Fig. 4 Two-dimensional slice of 17-factor RAM DOE test blocks.

After data collection for each block, the RAM algorithm generates new aerodynamic models using stepwise regression [24, 35] or multivariate orthogonal function modeling [24, 36] for model structure identification and ordinary least-squares regression for parameter estimation. The candidate regressor complexity reflects the current amount of available data, with more complex models becoming identifiable when additional data are available. The model identification methodology will be discussed further in the next section, along with special considerations for reduced-order modeling using computational testing.

After a candidate aerodynamic model has been developed for a given amount of data, the model adequacy is tested using a prediction error test to determine if the user’s desired level of modeling fidelity has been achieved. Regression methods minimize the summation of squared modeling residuals between modeled and measured response, so inspection of modeling fit metrics and modeling residuals alone does not provide information about the model predictive capability. Assessment of model performance using validation data not used for modeling provides a more reliable estimate of model prediction accuracy. Validation assessment can be performed by analyzing the residuals between the measured response z and predicted response $\hat{y}$ for the same explanatory variable inputs. Comparison of modeling and prediction residuals is useful because a significant increase in the spread of prediction residuals compared to modeling residuals is a way of diagnosing an improper model fit. Residuals can be given further interpretability by normalization. The error normalization metric used in this work is the range of response variable measurements used to develop the model. The normalized residual vector is defined as:

$$e^* = \frac{z - \hat{y}}{\text{range}(z)} \tag{2}$$

The critical binomial analysis of residuals prediction error metric (e^*_{cv}) is most often used to quantify the aggregate prediction error in the RAM algorithm. The process of computing e^*_{cv} is shown in Ref. [13] and further explanation of critical binomial analysis of residuals and justification for using this metric to assess prediction error is given in Ref. [37]. Alternatively, the normalized root-mean-square error (NRMSE),

$$\text{NRMSE} = \frac{1}{\text{range}(z)} \sqrt{\frac{(z - \hat{y})^T \, (z - \hat{y})}{N}} \tag{3}$$

for validation data can be used to quantify the aggregate prediction error. The prediction error is calculated for each response variable to quantify model performance and is compared to the user-defined level of modeling fidelity. If each response passes the prediction error test, then the models are designated as complete and the modeling process ends with the RAM algorithm generating an output file containing the final aerodynamic model. If any response fails the prediction error test, the RAM process continues by acquiring more data and fitting new models. If additional test blocks are available for a particular modeling region, the algorithm will send the next test block to the test facility for data acquisition. If all designed test blocks have been exhausted, the RAM algorithm partitions the modeling space for a user-specified test factor and new data is collected for each new region. Modeling can also be ceased by user intervention if the models are deemed sufficient by, for example, only failing the prediction error test by a small margin or only failing the prediction error test in certain response variables.

Model partitioning is a critical step in the RAM process for modeling complex vehicle aerodynamics over a large factor range. For many aerodynamic modeling studies, there can be nonlinear behavior that is difficult to adequately capture with a single polynomial fit. In order to sufficiently describe this complexity and reduce overall modeling error, the RAM algorithm is designed to partition the modeling space and develop new models over a smaller range of certain factors. The RAM splitting process is demonstrated in Fig. 5a for a single test factor, where local models are defined on each interval, or region, shown in the figure. Passing regions are shown in green and failing regions are shown in red. When the identified models in a certain region fail to meet the prediction error threshold after all test blocks have been completed, the region is split, new data is collected, and new models are fit until the desired prediction error is achieved. Upon obtaining passing modeling regions over the full modeling space, the modeling process is deemed complete. However, the individual models covering a subset of the factor space usually do not perfectly intersect with neighboring models at their boundaries, which creates a discontinuity between modeling regions. This is an undesirable attribute for simulation and controls applications. In order to blend neighboring models, the RAM software utilizes data from regions on both sides of the model intersection to create additional blending models spanning over the local intersections. This process is reflected in Fig. 5b, where the set of passing region models are shown in green and the models used for blending are shown in blue. The regions of overlap between local models are then smoothly combined using a quintic transition polynomial weighting function, following the procedure described in Ref. [15]. This model blending approach allows for a globally smooth response surface over the whole modeling space.

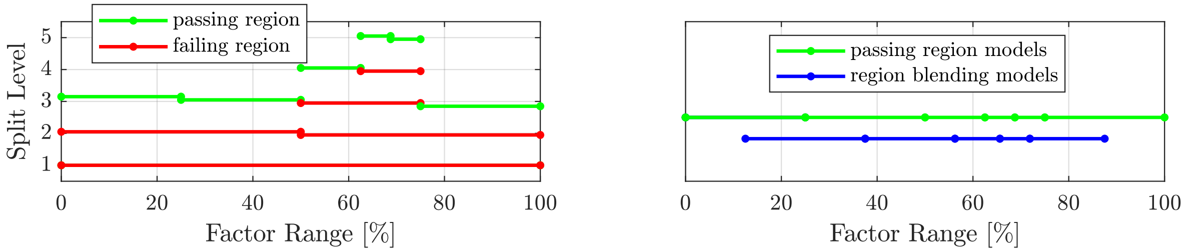

(a) Example RAM region splitting **(b) Example RAM region blending**

Fig. 5 Demonstration of RAM splitting and model blending logic, with local models defined on each interval.

IV. Model Identification Methodology

The following subsections provide an overview of the model structure determination and parameter estimation methods utilized within the RAM algorithm. A comprehensive description of these techniques is given in Ref. [24]. The model identification methods used in the RAM software were adapted from the System IDentification Programs for AirCraft (SIDPAC) software toolbox.[†] SIDPAC is a collection of programs written in MATLAB® that can be tailored for a particular modeling effort. This flexibility was beneficial while developing the RAM software.

A. Parameter Estimation

Ordinary least-squares regression is used to estimate a vector of n_p unknown model parameters in a vector $\boldsymbol{\theta}$ for a given model $\boldsymbol{y} = \boldsymbol{X}\boldsymbol{\theta}$ [24]. Here $\boldsymbol{y}$ is the length N model response vector and $\boldsymbol{X}$ is a $N \times n_p$ matrix consisting of column vectors of regressors assumed to be assembled from data that are measured without error. The regression equation, including a measurement of the response variable $\boldsymbol{z}$, corrupted by constant variance, zero-mean, and uncorrelated measurement error $\boldsymbol{\nu}$, is given as:

$$\boldsymbol{z} = \boldsymbol{X}\boldsymbol{\theta} + \boldsymbol{\nu} \tag{4}$$

For least-squares parameter estimation, the optimal estimate of the unknown parameters $\boldsymbol{\theta}$ is determined by minimizing the cost function:

$$J(\boldsymbol{\theta}) = \frac{1}{2}\left(\boldsymbol{z} - \boldsymbol{X}\boldsymbol{\theta}\right)^T \left(\boldsymbol{z} - \boldsymbol{X}\boldsymbol{\theta}\right) \tag{5}$$

It follows that the solution to compute an optimal estimate of the unknown parameters is

$$\hat{\boldsymbol{\theta}} = \left(\boldsymbol{X}^T\boldsymbol{X}\right)^{-1}\boldsymbol{X}^T\boldsymbol{z} \tag{6}$$

where $\hat{\boldsymbol{\theta}}$ is a vector of n_p estimated parameters. Assuming uncorrelated measurement errors and an adequate model structure is used to compute a modeled response variable history $\hat{\boldsymbol{y}} = \boldsymbol{X}\hat{\boldsymbol{\theta}}$, a length n_p vector of standard errors $\boldsymbol{s}(\hat{\boldsymbol{\theta}})$ corresponding to the estimated parameters $\hat{\boldsymbol{\theta}}$ is given as:

$$\boldsymbol{s}(\hat{\boldsymbol{\theta}}) = \sqrt{\left(\frac{\left(\boldsymbol{z} - \hat{\boldsymbol{y}}\right)^T\left(\boldsymbol{z} - \hat{\boldsymbol{y}}\right)}{N - n_p}\right)\mathrm{diag}\left[\left(\boldsymbol{X}^T\boldsymbol{X}\right)^{-1}\right]} \tag{7}$$

The present work involves model identification from computational testing, where both the explanatory variables and response variables contain no measurement error. Stated another way, the test results are purely deterministic, meaning that if a certain combination of factor settings is replicated, an identical measured response will be recorded. Perfect explanatory variable measurements aid accurate parameter estimation, since regression methods assume that the regressors are known without error. Perfect response data, however, results in modeling residuals derived solely from modeling errors, which are generally not normally distributed, constant variance, and independent. While the parameter estimates obtained from least-squares regression are still valid, the parameter standard errors, parameter confidence intervals, and model prediction intervals lack statistical justification; parameter significance testing is also not justified.

Least-squares regression estimates model parameters in a fixed model structure. Consequently, a method of determining an adequate model structure is required.

B. Model Structure Determination

Development of an adequate model structure is one of the most challenging aspects of aero-propulsive modeling for eVTOL aircraft. These vehicles share overlapping characteristics with both fixed-wing and rotary-wing aircraft, as well as experience complex vehicle-specific phenomena such as high incidence angle propulsor aerodynamics, distributed propulsion interactions, and propulsion-airframe interactions, which must be represented in the model structure. Consequently, suitable definitions of modeling explanatory and response variables are unclear and the expected model structure is not well defined due to limited previous research in this area. Furthermore, the presence of a larger number of candidate regressors compared to conventional aircraft modeling problems leads to large data processing times, and a requirement for more subject matter expert insight. Additional challenges for computational experiment model structure selection arise because the response data have no random error, which means that modeling residuals are derived only from modeling error. Multiple techniques were investigated to develop the model structure,

---

[†] Information available online at https://software.nasa.gov/software/LAR-16100-1 [accessed May 2021]

including stepwise regression [24, 35] and multivariate orthogonal function modeling [24, 36]. Each technique was found to require special procedures for the analysis presented in this paper to account for the response data lacking random error.

1. Stepwise Regression

The stepwise regression algorithm used in this work for model structure development is based on the algorithm described in Refs. [24, 35]. This algorithm is a combination of forward selection and backwards elimination of candidate regressors where a single regressor is either added to or removed from the model at each iteration. The procedure is started with only a bias parameter included in the model structure. The first step is adding the candidate regressor with the highest correlation to the unmodeled portion of the response variable into the model. The process is continued by adding excluded candidate model terms with the highest partial correlation r_i into the model, for the conditioned modeling problem. For the ith model term excluded from the model structure, r_i is calculated as:

$$r_i = \frac{(\boldsymbol{v}_i - \bar{v}_i)^T (\boldsymbol{v}_z - \bar{v}_z)}{\sqrt{(\boldsymbol{v}_i - \bar{v}_i)^T (\boldsymbol{v}_i - \bar{v}_i)}\sqrt{(\boldsymbol{v}_z - \bar{v}_z)^T (\boldsymbol{v}_z - \bar{v}_z)}} \tag{8}$$

Here, $\boldsymbol{v}_i$ is the ith model term residual vector resulting from being regressed on by terms included in the current model, with mean denoted $\bar{v}_i$; $\boldsymbol{v}_z$ is the difference between the measured response variable and the response modeled by the current regressors in the model, with mean denoted $\bar{v}_z$.

At each stepwise regression iteration, terms included in the model are considered to be removed from the model if their partial F-statistic, F_{0_i}, falls below a cutoff threshold $F(\alpha_p, 1, N - n_p)$ prescribed by a partial F-test for significance at an α_p significant level with n_p included model regressors. The significant level α_p is commonly chosen as $\alpha_p = 0.05$, or 95% confidence that the model term is significant. For the ith model term included in the current iteration of the model structure, F_{0_i} is calculated as

$$F_{0_i} = \frac{\hat{\theta}_i^2}{s^2(\hat{\theta}_i)} \tag{9}$$

where $\hat{\theta}_i$ is the associated parameter estimate and $s^2(\hat{\theta}_i)$ is the respective parameter variance.

The stepwise regression algorithm can be run automatically or manually. Due to the abundance of candidate regressors and large number of model terms needed to describe complex eVTOL aerodynamic phenomena, each model required many iterations to converge to an adequate model structure. For this reason, the stepwise regression algorithm was run automatically until the remaining excluded model terms did not surpass the partial F-statistic cutoff value when added to the model.

2. Multivariate Orthogonal Function Modeling

The multivariate orthogonal function (MOF) modeling approach described in Refs. [24, 36] is initiated by orthogonalizing a predefined set of candidate regressors using an algorithm such as Gram-Schmidt orthogonalization or QR decomposition. Orthogonal regressors are convenient for model structure development because of the ability to independently assess the orthogonalized candidate regressors potential to model the response variable—this facilitates selecting only the model terms that significantly contribute to model effectiveness. The orthogonal regressors are then ranked from highest to lowest decrease in the mean squared fit error (MSFE):

$$\text{MSFE} = \frac{1}{N}(\boldsymbol{z} - \hat{\boldsymbol{y}})^T (\boldsymbol{z} - \hat{\boldsymbol{y}}) \tag{10}$$

In other words, this ranks the regressors from highest to lowest ability to improve the model. Candidate regressors are brought into the model structure in this order.

Deciding which terms to include in the final model can then be done using one or more statistical metrics. A common threshold for MOF modeling is to minimize the predicted squared error (PSE) [24, 38]. The PSE is the sum of the MSFE and a model complexity penalty related to the number of terms included in the model,

$$\text{PSE} = \text{MSFE} + \sigma_{max}^2 \frac{p}{N} \tag{11}$$

where p is the number of terms in the current model structure and σ_{max}^2 is an estimate of the upper-bound of mean squared error for the model prediction of data not used to develop the model. In physical testing, the quantity σ_{max}^2 can be estimated using the variance of measured responses between repeated data points or from the variance between the measured response z and mean measured response $\bar{z}$. In the present application where the response of repeat points is identical, the latter approach is used to provide an estimate of σ^2_{max} as:

$$\sigma^2_{max} = \frac{1}{N-1} \sum_{i=1}^{N} [z(i) - \bar{z}]^2 \tag{12}$$

After the orthogonal regressors were ranked by their ability to reduce the MSFE, the cutoff for model term addition was chosen to be the candidate model term where the PSE was minimized. After determining the model terms to include in the model structure, the final parameter values were estimated using least-squares regression in ordinary regressor space.

3. Deterministic Experiment Considerations

As highlighted previously, the data used for model development in this paper is obtained from computational experiments where the response data do not contain measurement error, and consequently, replicate factor settings will produce the same output response. This results in several practical challenges for model structure determination. Preliminary model structure identification results showed that stepwise regression run with a common significant level threshold (e.g. $\alpha_p = 0.05$) admitted too many model terms and MOF modeling run using the PSE as defined in Eqs. (11)-(12) admitted too few model terms. Both over-fitting and under-fitting models results in deficient response prediction. These observations were made by subject matter expert review of the model terms and consulting modeling and prediction error metrics in view of the number of included model terms.

Stepwise regression relies on significant testing for each candidate model term to iteratively converge to a final model structure. The partial F-statistic (Eq. (9)) is used as the cutoff threshold to retain terms in the model; however, its value is dependent on the estimated parameter variance $s^2(\hat{\theta}_i)$, which is not statistically valid because the residuals only contain modeling error (which is generally not normally distributed, constant variance, and independent). Although, for the present study, the residuals appeared to be reasonably normally distributed, constant variance, and independent, even though the residuals only contain modeling error. An example residual analysis is shown later in Sec. VII. The CFD simulations run using randomized DOE test matrices include implicit variability between data points from sources such as complex flowfields, flow unsteadiness, convergence criteria, grid resolution, and turbulence models. Accordingly, reduced-order model identification for the CFD simulations used in this application results in approximately independent, normally distributed, and constant variance modeling residuals, which can be justified by the central limit theorem. This implies that use of the partial F-statistic still provides a valid metric to assess the relative utility of including a particular model term. As a consequence of the noise-free experiment, commonly-applied significance level thresholds were found to admit too many model terms into the model. Over-parameterizing the model is undesirable because the model yields unrealistic response predictions and unnecessary curvature. To mitigate this problem, model structures identified with several different significance levels between $\alpha_p = 0.05$ (95% confidence) to $\alpha_p = 10^{-6}$ (99.9999% confidence) were identified and compared. For the data analyzed for this work, $\alpha_p = 0.0001$ (99.99% confidence) appeared to be a good choice to obtain a parsimonious model with good prediction capability.

While the PSE metric and the overall MOF modeling process do not have underlying assumptions regarding the probability distribution of modeling residuals, the resulting model structure is largely dependent on the estimate of σ^2_{max}. For this work, the PSE metric threshold defined using the σ^2_{max} calculated using Eq. (12) was found to admit too few model terms into the model, which failed to sufficiently describe certain important, deterministic aerodynamic characteristics. In other words, the σ^2_{max} value, calculated using Eq. (12), is overestimated for the present application and, thus, its use within the PSE metric make the PSE-based model term entry threshold too conservative. To overcome this shortcoming, the σ^2_{max} estimate used to calculate the PSE was multiplied by a scale factor κ, to allow admission of more model terms. The PSE metric, with this modified prediction error variance estimate, is calculated as:

$$\text{PSE} = \text{MSFE} + \kappa \sigma^2_{max} \frac{p}{N} \tag{13}$$

Model structures developed using MOF modeling with several different values of κ between $\kappa = 1$ (equivalent to the standard σ^2_{max} formulation) to $\kappa = 0.05$ were identified and compared. For the data analyzed for this work, $\kappa = 0.2$ appeared to be a good choice to identify a model with good prediction capability, while maintaining model parsimony.

The model structures identified using the above cutoff criteria for stepwise regression and MOF modeling yielded models with good prediction capability and a reasonable number of model terms. Although similar results were obtained using both methods and the use of both methods has been justified for the present application, MOF modeling is the more generally applicable algorithm due to fewer assumptions regarding the residual distribution. For this reason, the models identified using MOF modeling with a model complexity penalty scale factor of $\kappa = 0.2$ were taken as the final models.

Although not applied in this work, it is worth noting that an alternative approach to identify an adequate model structure from a noise-free experiment could be to inject Gaussian white noise into the response data representative of the noise levels expected to be seen in a physical measurement facility, such as a wind tunnel. With response data containing representative measurement noise, stepwise regression and multivariate orthogonal function modeling can be run without the above modifications to identify the model structure. Once the model structure is identified, parameter estimation could then be performed using the noise free data to prevent the noise from corrupting the final parameter estimates. While this is a valid alternative approach, the final model structure will still be dependent on the variance of the injected noise, which is effectively another tunable scale factor.

V. Computational Testing

While wind tunnel and flight testing provide high-quality data needed for aerodynamic model development, these methods also require significant time and resources, including development of a physical test vehicle. Alternatively, computational testing does not require any vehicle hardware, allowing aerodynamic analysis in early design stages. For this work, CFD simulations are used as a *computational test facility* to enable aero-propulsive model development for the conceptual Lift+Cruise aircraft. Specifically, the OVERFLOW CFD code [39–41] was used with the Chimera overset grid approach to produce the results presented in this paper. The Chimera overset grid approach is particularly suited to multiple-body or moving body applications, and has been used extensively for rotorcraft and eVTOL configurations [42, 43]. The complex, nonlinear aerodynamics and vehicle interactions exhibited by eVTOL aircraft warrant investment in computationally expensive CFD solutions to develop aero-propulsive models with reasonable prediction capability. For the Lift+Cruise aircraft, rotor wash over the wing and tail can make a large contribution to the vehicle aerodynamics. These effects are apparent in the flowfield depicted in Fig. 6.

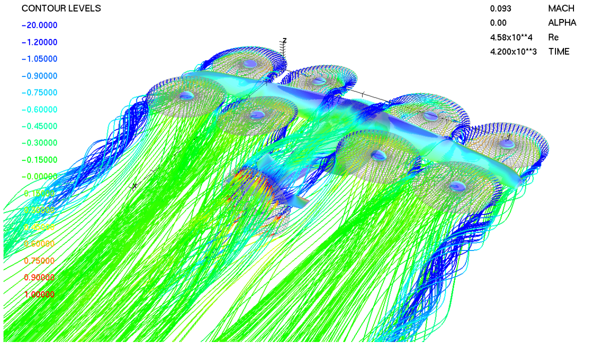

Fig. 6 Transitioning Lift+Cruise vehicle with flow from the rotors colored by pressure coefficient.

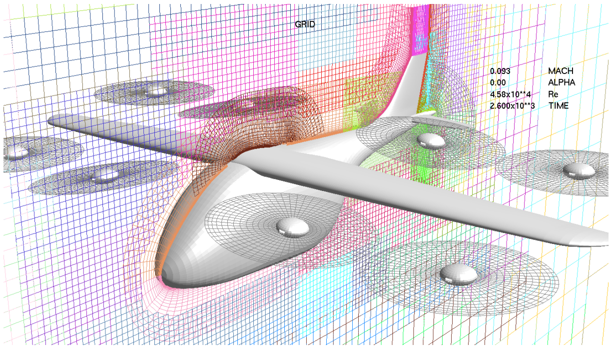

Fig. 7 CFD overset grid system for the Lift+Cruise vehicle.

A coarse computational grid of four million points was created for the Lift+Cruise concept aircraft analyzed in this work to facilitate developing an aero-propulsive model of the vehicle sufficient for flight dynamics simulations. The aircraft components included in the gridding were the wing, fuselage, horizontal tail, vertical tail, eight lifting rotors, and pusher propeller, as shown in Fig. 7. The rotors and pusher propeller were modeled using a rotor disk methodology [44], as opposed to modeling fully rotating blades, to reduce the grid size and encourage steady-state flow solutions. The aircraft geometry was also simplified by removing the support struts for the lifting rotors and the landing gear. Further simplification of gridding requirements was achieved by deforming the surface grids to model control surfaces and ignoring the gaps at the ends of each control surface. The present grid system is adequate to model dominant propulsion-airframe interaction effects, however, grid refinement studies and unsteady flow simulations were not performed. While these simplifications are justified for the current study using a conceptual vehicle, certain complexity reduction measures would need to be reassessed for modeling an actual aircraft. With these approximations, each test point was calculated in approximately two hours on one node (20 CPU cores) of the NASA Advanced Supercomputing (NAS) Pleiades system. Typical runs were made generating 50 test points simultaneously, limited by availability of resources on the system.

The computational expense associated with CFD simulations currently requires a significant amount of time to compute aerodynamic force and moment predictions at a single point. Thus, in order to develop an effective and efficient flight dynamics simulation, response surface representations of the complex Lift+Cruise aerodynamics were identified using the RAM software. The general process for computational data collection used for model development was initiated by developing a test matrix using the RAM software, which specified the freestream velocity components, control surface deflection angles, and propulsor speed settings for each test point. The RAM algorithm subsequently generated a text file listing factor settings for each point in a test block. Specialized scripts were used to generate OVERFLOW input files and modify computational geometry to match each test point. CFD simulations were then run to predict the aero-propulsive forces and moments for each point, and additional scripts extracted vehicle force and moment history data to generate average values. The results were collected into text files read by the RAM software and utilized to develop response surface models describing the aircraft aerodynamics following the RAM algorithm. This process, depicted in Fig. 8, continued until models with sufficient prediction capability had been identified.

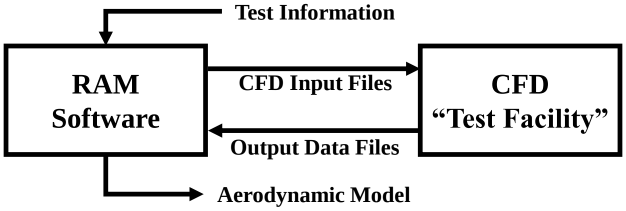

Fig. 8 Connection of the RAM algorithm with the OVERFLOW CFD test facility.

VI. Lift+Cruise Aero-Propulsive Modeling Approach

The Lift+Cruise aircraft has numerous different operational flight conditions where drastically different flight characteristics are expected. In low-speed flight, the aircraft is expected to exhibit rotorcraft and multirotor like aerodynamics. In high-speed forward flight, the vehicle's aerodynamics are expected to resemble a fixed-wing aircraft. In transition, a hybrid of fixed-wing and rotary-wing aerodynamic characteristics are anticipated. In order to develop a flight dynamics simulation for the vehicle's full flight envelope, it is necessary to model all flight conditions expected to be seen through a typical flight mission. As mentioned previously, propulsion and airframe aerodynamics for eVTOL aircraft are generally highly coupled across a significant portion of their flight envelope. Therefore, in the context of modeling the Lift+Cruise aircraft, the aerodynamic model describes propulsion and airframe aerodynamic characteristics in an integrated aero-propulsive model.

The Lift+Cruise flight envelope was divided into four distinct flight regimes for model development based on which control effectors were active. The *hover regime* occurs in low-speed flight where all lifting rotors are active, but the pusher propeller is off. This would resemble when the vehicle is close to takeoff or landing. The *transition regime* occurs when the aircraft is moving between low-speed hover and forward flight. In this case, both the lifting rotors and pusher propeller are active. The *cruise regime* occurs when the aircraft is operating in forward flight propelled by only the pusher propeller. The *glider regime* simulates a failure condition when both the lifting rotors and pusher propeller are inactive. The full range of test factors prescribed for each flight regime is shown in Tables 1-4. The forward speed ranges that each of these flight regimes cover are shown in Fig. 9. The full RAM block designs described in Sec. III for the cruise and glider regimes supported up to cubic and three-factor interaction model terms; the full RAM block design for the hover and transition flight regimes only supports up to pure cubic and two-factor interactions model terms due to the large number of test factors.

The test factors varied for the computational experiments included the body-axis velocity components u, v, w, control surface deflections $\delta_{a_L}, \delta_{a_R}, \delta_{e_L}, \delta_{e_R}, \delta_r$, and propulsor speed $n_1, n_2, ..., n_9$. While the pusher propeller for the Lift+Cruise design is variable-pitch, the propeller was held to a fixed pitch angle for the present modeling work. For the cruise and glider flight regimes, the test matrices were developed in terms of α and β rather than v and w. This reflects that the vehicle is essentially a fixed-wing aircraft in the cruise and glider flight regimes, and thus, the aerodynamics are more effectively described by airflow angles over a range of freestream velocities. Altitude effects were not considered for this study, although, it is understood that operation of the vehicle at different altitudes would significantly change the aero-propulsive model in certain flight regimes, depending on the model formulation. All computational testing for this

Table 1 Test factor ranges used for modeling the Lift+Cruise hover regime (16 variable factors)

Factor(s)	Units	Minimum	Center	Maximum
u	kts	−5	+20	+45
v	kts	−10	0	+10
w	kts	−10	0	+10
$\delta_{a_L}, \delta_{a_R}, \delta_{e_L}, \delta_{e_R}, \delta_r$	deg	−30	0	+30
$n_1, n_2, ..., n_8$	RPM	550	1050	1550
n_9	RPM	0	0	0

Table 2 Test factor ranges used for modeling the Lift+Cruise transition regime (17 variable factors)

Factor(s)	Units	Minimum	Center	Maximum
u	kts	−5	+45	+95
v	kts	−10	0	+10
w	kts	−10	0	+10
$\delta_{a_L}, \delta_{a_R}, \delta_{e_L}, \delta_{e_R}, \delta_r$	deg	−30	0	+30
$n_1, n_2, ..., n_8$	RPM	550	1050	1550
n_9	RPM	750	1250	1750

Table 3 Test factor ranges used for modeling the Lift+Cruise cruise regime (9 variable factors)

Factor(s)	Units	Minimum	Center	Maximum
u	kts	+50	+90	+130
β	deg	−6	0	+6
α	deg	0	+6	+12
$\delta_{a_L}, \delta_{a_R}, \delta_{e_L}, \delta_{e_R}, \delta_r$	deg	−30	0	+30
$n_1, n_2, ..., n_8$	RPM	0	0	0
n_9	RPM	550	1150	1750

Table 4 Test factor ranges used for modeling the Lift+Cruise glider regime (8 variable factors)

Factor(s)	Units	Minimum	Center	Maximum
u	kts	+50	+90	+130
β	deg	−6	0	+6
α	deg	0	+6	+12
$\delta_{a_L}, \delta_{a_R}, \delta_{e_L}, \delta_{e_R}, \delta_r$	deg	−30	0	+30
$n_1, n_2, ..., n_8$	RPM	0	0	0
n_9	RPM	0	0	0

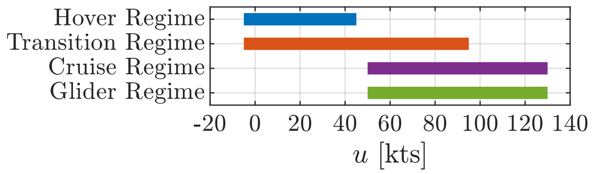

Fig. 9 Forward speed range modeled for each Lift+Cruise flight regime.

work was performed assuming standard atmosphere conditions at an altitude of 6000 ft.

After collection of computational data, models were fit using the RAM software. The explanatory and response variables used for eVTOL aircraft system identification are currently not well established in literature. Reference [13] justified the use of body-axis velocity components, control surface deflection angles, and either propulsor rotational speed or estimated propulsor thrust as the explanatory variables for modeling a tilt-wing, distributed propulsion aircraft. This same work justified using dimensional body-axis forces and moments as the response variables. These modeling choices could also be used to model the Lift+Cruise, but the different vehicle configuration suggests a modified modeling strategy.

For the Lift+Cruise hover regime, the explanatory variables were defined as the body-axis velocity components u, v, w, control surface deflections $\delta_{a_L}, \delta_{a_R}, \delta_{e_L}, \delta_{e_R}, \delta_r$, and rotor speed $n_1, n_2, ..., n_8$. The explanatory variables defined for the transition regime were identical to those define for the hover regime, except propeller speed n_9 was also included. The response variables were designated as the dimensional body-axis aero-propulsive forces X, Y, Z and moments L, M, N. Dimensional forces and moments are used opposed to force and moment coefficients because nondimensionalization by freestream dynamic pressure $\bar{q}$ is not valid for vehicles that are propulsion-dominated and experience significant airframe-propulsion interaction. Propulsor aerodynamics, for example, scale with the dynamic pressure experienced by the individual propeller blades opposed to freestream dynamic pressure. The use of body-axis velocity as explanatory variables and dimensional forces and moments as response variables also allows the model to be defined at a zero-airspeed hover condition.

In the Lift+Cruise cruise and glider regimes, the aircraft aerodynamic characteristics become similar to a fixed-wing vehicle. Consequently, airflow angles α and β are used as explanatory variables for these flight conditions opposed to body-axis velocity components. Also, the response variables are defined as the dimensionless force coefficients C_x, C_y, C_z and moment coefficients C_l, C_m, C_n, shown in Eq. (1). Lift coefficient C_L and drag coefficient C_D could be used as response variables instead of C_x and C_z, but this choice did not appear to make a significant difference in model performance because cruise and glider modeling was only performed over a modest angle of attack range. As before, the control surface deflections $\delta_{a_L}, \delta_{a_R}, \delta_{e_L}, \delta_{e_R}, \delta_r$ are defined as additional explanatory variables. For the cruise model, the pusher propeller rotational speed n_9 could be used as an explanatory variable, however, the variable does not have a widely-used dimensionless form compatible with using the body-axis force and moment coefficients as the response variables. Advance ratio,

$$J = \frac{V}{nD} \tag{14}$$

is commonly used to parameterize axial-flow propeller aerodynamics using the propeller thrust coefficient, $C_T = \frac{T}{\rho n^2 D^4}$, and torque coefficient, $C_Q = \frac{Q}{\rho n^2 D^5}$, as the response variables; advance ratio parameterization can be also justified here using dimensional analysis [45]. However, parameterizing propulsion effects with a polynomial expansion of advance ratio when using the aircraft force and moment coefficients as response variables is not physically consistent. The force and moment coefficients are normalized by freestream dynamic pressure $\bar{q} = \frac{1}{2}\rho V^2$, rather than ρn^2, which is proportional to the dynamic pressure experienced by the individual propeller blades. Geometric constants used for normalization of the airframe and propeller response variables are also different, but these are constant for a particular aircraft rather than a variable quantity.

To derive a more physically-justified dimensionless variable to describe the pusher propeller effect on the aircraft force and moment coefficients, consider a model for the propeller thrust coefficient quadratic in advance ratio:

$$C_T = C_{T_o} + C_{T_J} J + C_{T_{J^2}} J^2 = C_{T_o} + C_{T_J} \left(\frac{V}{nD}\right) + C_{T_{J^2}} \left(\frac{V}{nD}\right)^2 \tag{15}$$

Converting this model to dimensional thrust T using the definition of thrust coefficient yields:

$$T = \rho n^2 D^4 \left[C_{T_o} + C_{T_J} \left(\frac{V}{nD} \right) + C_{T_{J^2}} \left(\frac{V}{nD} \right)^2 \right] = \rho D^2 \left(C_{T_o} D^2 n^2 + C_{T_J} DnV + C_{T_{J^2}} V^2 \right) \tag{16}$$

Since D is vehicle constant and air density ρ is constant at a particular atmospheric test condition, the model terms are essentially n^2, nV, and V^2 in the dimensional model. Note that these terms appear as candidate regressors for the dimensional modeling approach used for the transition flight regime when quadratic and two-factor interactions model terms are supported by the data and assuming $V \approx u$. For the thrust component oriented along the body x-axis, the propulsion component of the body x-axis force coefficient C_{x_p} (cf. Eq. (1)) can be written as:

$$C_{x_p} = \frac{T}{\frac{1}{2}\rho V^2 S} = \frac{2D^2}{S} \left[C_{T_o} \left(\frac{nD}{V} \right)^2 + C_{T_J} \left(\frac{nD}{V} \right) + C_{T_{J^2}} \right] \tag{17}$$

The quantity nD/V is the inverse of advance ratio, which is defined here as:

$$\hat{J} = \frac{nD}{V} \tag{18}$$

Absorbing the constant terms into the model parameters, the propulsion component of x-axis force coefficient can be written as,

$$C_{x_p} = C_{x_{\hat{J}^2}} \hat{J}^2 + C_{x_{\hat{J}}} \hat{J} + C_{x_{po}} \tag{19}$$

where $C_{x_{\hat{J}^2}} = \frac{2D^2}{S} C_{T_o}$, $C_{x_{\hat{J}}} = \frac{2D^2}{S} C_{T_J}$, and $C_{x_{po}} = \frac{2D^2}{S} C_{T_{J^2}}$.

Following the results of this analysis, the explanatory variable for the pusher propeller in the cruise regime is defined to be $\hat{J}_9 = n_9 D/V$, which resulted in the best model fit. Note that this approach is only valid when the vehicle is operating like a fixed-wing airplane, although, airframe-propulsion interactions are still able to be described by the model. Also note that the $C_{x_{po}} = \frac{2D^2}{S} C_{T_{J^2}}$ term in Eq. (19) will not be separately identifiable from the aerodynamic bias C_{x_o} when airframe and propulsion aerodynamics are being estimated together.

The explanatory variables and response variables defined for each flight regime are summarized in Table 5. The following section presents sample modeling results using this methodology.

Table 5 Summary of explanatory variables and response variables for the different flight regimes

Hover Regime	
Explanatory Variables	$u, v, w, \delta_{a_L}, \delta_{a_R}, \delta_{e_L}, \delta_{e_R}, \delta_r, n_1, n_2, n_3, n_4, n_5, n_6, n_7, n_8$
Response Variables	X, Y, Z, L, M, N
Transition Regime	
Explanatory Variables	$u, v, w, \delta_{a_L}, \delta_{a_R}, \delta_{e_L}, \delta_{e_R}, \delta_r, n_1, n_2, n_3, n_4, n_5, n_6, n_7, n_8, n_9$
Response Variables	X, Y, Z, L, M, N
Cruise Regime	
Explanatory Variables	$u, \beta, \alpha, \delta_{a_L}, \delta_{a_R}, \delta_{e_L}, \delta_{e_R}, \delta_r, \hat{J}_9$
Response Variables	$C_x, C_y, C_z, C_l, C_m, C_n$
Glider Regime	
Explanatory Variables	$u, \beta, \alpha, \delta_{a_L}, \delta_{a_R}, \delta_{e_L}, \delta_{e_R}, \delta_r$
Response Variables	$C_x, C_y, C_z, C_l, C_m, C_n$

VII. Aero-Propulsive Modeling Results

Separate aero-propulsive models were developed for each flight regime described above to produce a full-envelope aerodynamic database for the Lift+Cruise aircraft. For this study, the goal was to develop models minimizing prediction error, where a value of approximately 5% or less of e_{cv}^* for each response was considered to be adequate based on analysis judgment. Following the decision logic in the RAM algorithm, the hover and transition flight regimes were partitioned into two and five regions in u, respectively, to obtain adequate prediction capability. These steps are depicted in Fig. 10. After developing local models in each region, a global hover model and transition model was developed following the model blending process described in Sec. III with support from Ref. [15]. Adequate model performance within the cruise and glider flight regimes was obtained without requiring partitioning. This is because most of the aerodynamic variation with forward airspeed is described by modeling the response using the nondimensional aerodynamic force and moment coefficients, and the model was developed over a limited range of angle of attack.

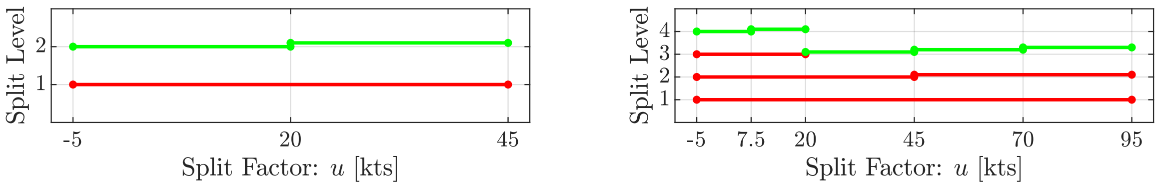

(a) Hover regime

(b) Transition regime

Fig. 10 RAM model partitioning steps in u needed to adequately model the Lift+Cruise hover and transition regimes.

A. Local Modeling Results

To analyze the adherence to regression modeling assumptions and analyze model adequacy, sample residual plots are shown in Fig. 11 for a local transition model for $45 \leq u \leq 70$ kts. Figure 11a shows the normalized modeling residuals and normalized validation residuals against run number, as well as the e_{cv}^* metric bounds. Figure 11b shows normal probability plots for the standardized modeling residuals for each response. Figure 11c shows the normalized modeling and validation residuals against the predicted response. These plots show that the residuals are reasonably independent, normally distributed, and constant variance which reflects the residual characteristics seen in physical testing, even though the data lacks measurement error. The identified model parameters are valid and significance testing can be used as a metric to assess the utility of including a particular model term; however, the parameter standard errors are not statistically meaningful. The plots also show that modeling and prediction residuals appear to have similar magnitude supporting the claim that a good predictive model has been identified. Residuals with similar character were obtained for local aero-propulsive models identified across the Lift+Cruise flight envelope.

Tables showing modeling and prediction error metrics for each local model within each flight regime are given at the end of this paper. Table 6 shows the coefficient of determination (R^2) value for each local model. The R^2 metric reflects the fraction of variation in the dependent variable about its mean value that is described by the model. All local models have an R^2 value above 93% and a majority of the local models have an R^2 value above 98% indicating that a significant portion of the variation in the response is described by the models. Table 7 shows the number of model terms identified in each local model and indicates that more model terms are required to model the hover and transition flight regimes due to the increased aerodynamic complexity present when the lifting rotors are operational. The binomial analysis of residuals prediction error metric (e_{cv}^*) value for each model is shown in Table 8. Most local models have an e_{cv}^* value less than 5% indicating that good models have been identified. Table 9 and Table 10 present the NRMSE for modeling and validation data, respectively. The NRMSE values calculated using modeling and validation data for each local model are similar also indicating that a quality model has been identified. The e_{cv}^* and NRMSE metrics are calculated using the response type used to identify the model (X, Y, Z, L, M, and N for hover and transition; C_x, C_y, C_z, C_l, C_m, and C_n for cruise and glider).

B. Global Modeling Results

The e_{cv}^* prediction error metric and validation NRMSE values for the global responses in each flight regime are compared in Fig. 12. The metrics are calculated using dimensional forces and moments such that all flight regimes

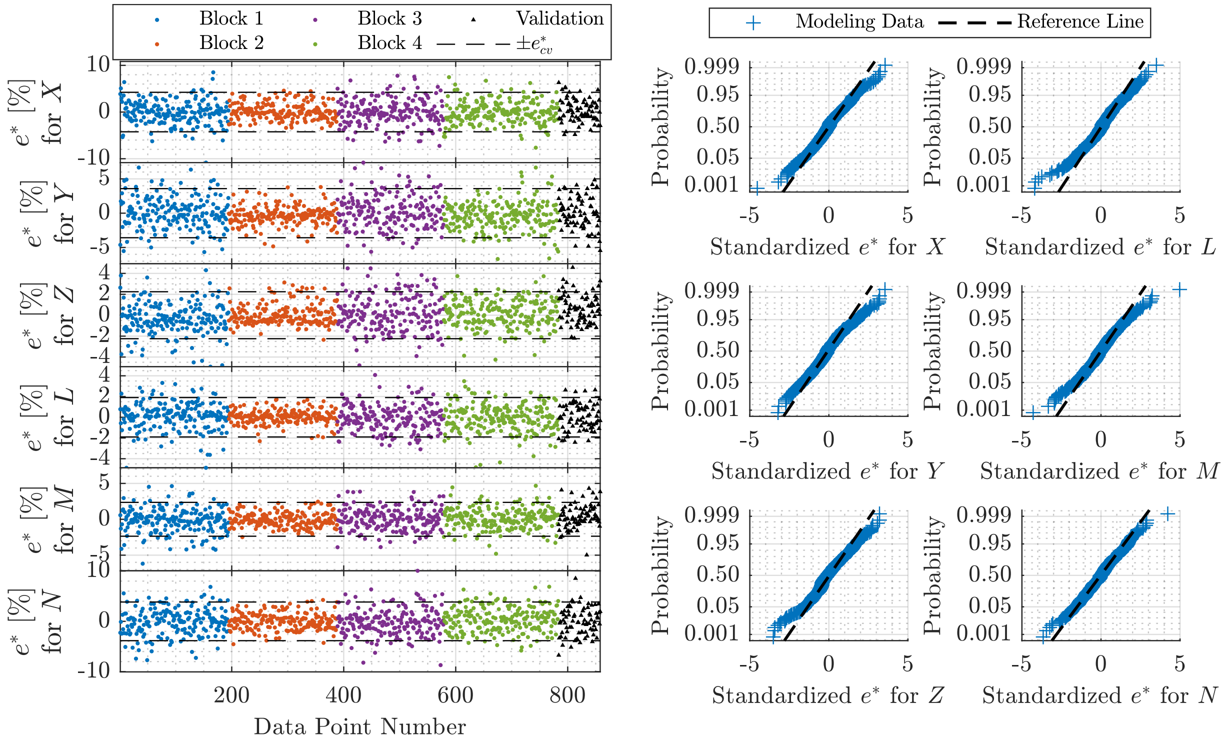

(a) Normalized residual history

(b) Normal probability plot

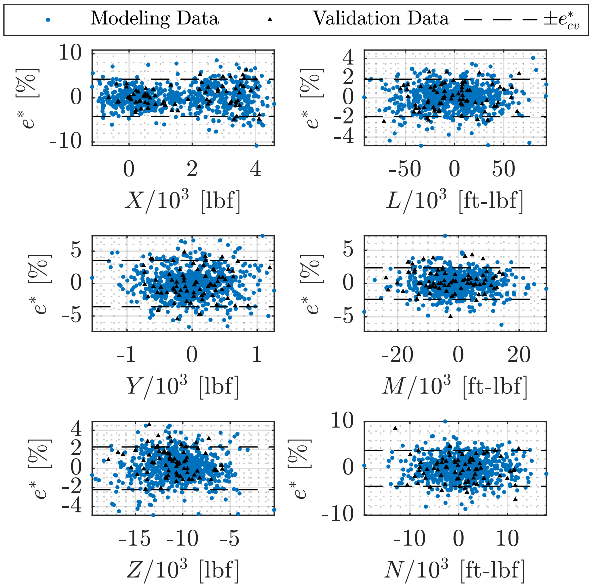

(c) Normalized residuals against predicted response

Fig. 11 Residual diagnostics for a local Lift+Cruise transition model ($45 \leq u \leq 70$ kts).

relative prediction error values can be directly compared. Almost all global prediction metrics values are 5% or lower indicating global models with adequate predictive capability were identified. For all responses except pitching moment, the transition and hover models have a higher prediction error compared to the cruise and glider models. This reflects the increased modeling difficulty for a lift+cruise aircraft in low-speed and transitioning flight due to highly nonlinear propulsion-airframe interactions (cf. Fig. 6).

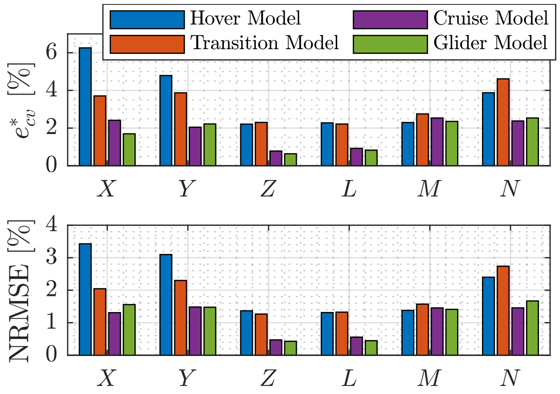

Fig. 12 Global e^*_{cv} and NRMSE values calculated using validation data for each response.

Figure 13 shows model response comparisons to one-factor-at-a-time (OFAT) sweeps in forward speed u for the hover, transition, and cruise flight regimes. Figure 13a and Fig. 13b show a u-sweep over a significant portion of the hover and transition flight regimes, where all other explanatory variables are set to their center values shown in Table 1 and Table 2, respectively. The model response shows overall good agreement with the OFAT data points, considering the substantial aerodynamic complexity exhibited in these flight regimes. Increased scatter in the CFD data points and a worse model fit for certain responses at low speeds (particularly for L and N) reflects the trade-off between efficiency and accuracy. A fixed number of time steps were used for all CFD runs in order to conduct efficient testing, rather than adapting the number of time steps for each run. Future studies may benefit from using an increased number of time steps at low speeds, where the nature of the flow physics leads to longer convergence times. Two u-sweeps for the cruise flight regime are shown in Fig. 13c at an angle of attack of 0° and 6° and a pusher propeller rotational speed n_9 of 1250 RPM and 1150 RPM, respectively; all other explanatory variables are held to their center values shown in Table 3. Close model predictions of the CFD data points can be seen for the X, Z, L, and M responses. Some model prediction deviations can be seen in the Y and N responses, but these responses are small and of lesser importance when sweeping u.

VIII. Flight Dynamics Simulation Considerations

The identified static aero-propulsive model for each flight regime is a central component of the flight dynamics simulation developed for the Lift+Cruise aircraft. However, there are additional components necessary for successful full-envelope flight simulations, which include isolated propulsor characterization, aerodynamic damping predictions, flight regime synthesis for full flight mission simulations, the equations of motion, and subsystem dynamics approximations. Each of these topics are briefly highlighted in the remainder of this section. The intended use of the developed Lift+Cruise simulation is intelligent contingency management research for eVTOL aircraft operating in a future urban flight environment [46].

A. Isolated Propeller and Rotor Model Development

Isolated propulsor model identification is useful for multiple purposes including aerodynamic damping predictions, flight regime synthesis, and propulsor failure approximations. For this work, different modeling strategies were used to develop a response surface representation for the forces and moments produced by the pusher propeller and lifting rotors. The conventional propeller variable normalization conventions (e.g. see Refs. [45, 47]) are used for both rotor and propeller model identification for simplicity, but it is recognized that rotors are generally modeled using a different geometric convention [48, 49]. Model predictions for the dimensional forces and moments are not dependent on whether the propeller or rotor normalization convention is used.

To develop an isolated rotor aerodynamic model, a blade element momentum theory (BEMT) simulation[‡] was used

---

[‡] The BEMT simulation used for this work was developed and validated by George Altamirano, Flight Dynamics Branch, NASA Langley Research Center; and David Hartman, Analytical Mechanics Associates, Hampton VA.

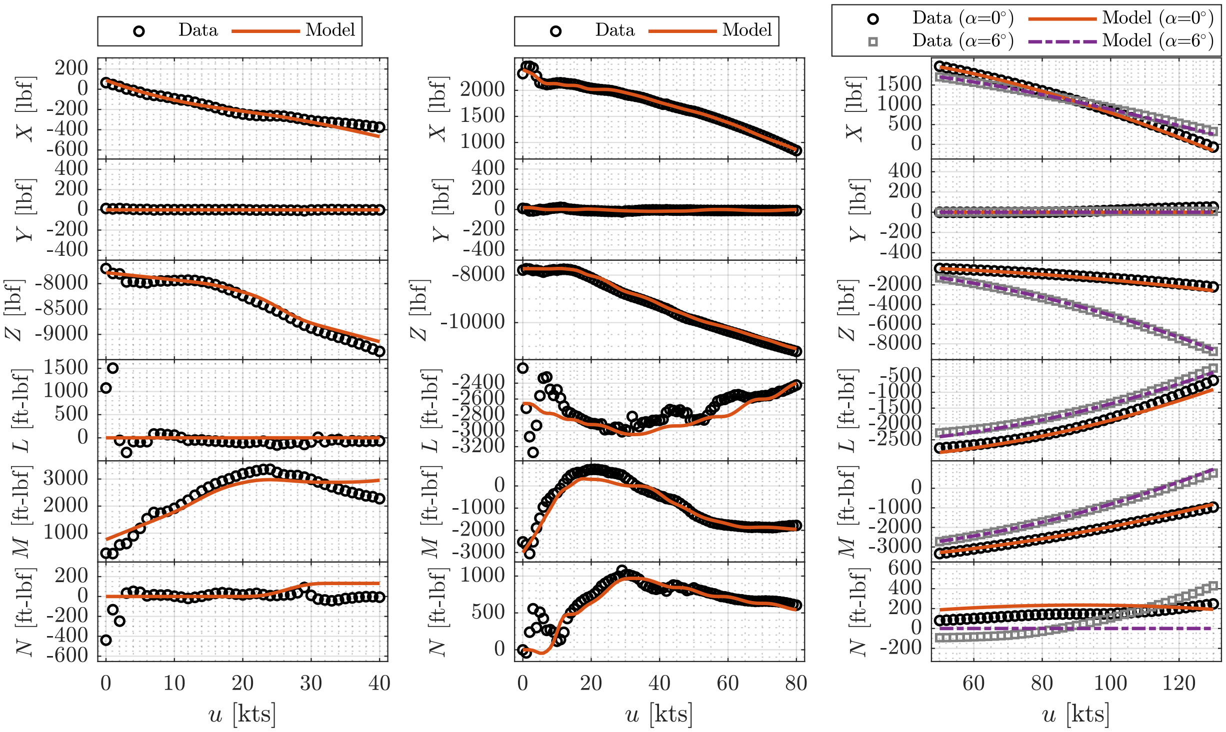

(a) Hover regime **(b) Transition regime** **(c) Cruise regime**

Fig. 13 Model response compared to CFD data points sweeping u.

as a computational test facility to identify a reduced-order response surface model for the dominant rotor aerodynamics. The BEMT simulation is based on an adapted form of the blade element calculations performed in the NDARC software[§] and predicts the forces and moments produced by the rotors operating at nonzero incidence angles. The reduced-order rotor aerodynamic modeling methodology followed similar modeling methods that is described in Ref. [15]. MOF modeling was used for model structure identification and ordinary least-squares regression was used for parameter estimation (see Sec. IV). The response variables were the propulsor force and moment coefficients in the hub frame,

$$C_{T_x} = \frac{T_x}{\rho n^2 D^4},\ C_{T_y} = \frac{T_y}{\rho n^2 D^4},\ C_{T_z} = \frac{T_z}{\rho n^2 D^4},\ C_{Q_x} = \frac{Q_x}{\rho n^2 D^5},\ C_{Q_y} = \frac{Q_y}{\rho n^2 D^5},\ C_{Q_z} = \frac{Q_z}{\rho n^2 D^5} \tag{20}$$

where T_x, T_y, T_z are the isolated propulsor forces and Q_x, Q_y, Q_z are the isolated propulsor moments in the propulsor hub frame. The explanatory variables were defined as the normal component of advance ratio J_x, tangential components of advance ratio J_z, and the tip Mach number M_{tip},

$$J_x = \frac{V \cos i_p}{nD} \tag{21}$$

$$J_z = \frac{V \sin i_p}{nD} \tag{22}$$

$$M_{tip} = \frac{\pi n D}{a} \tag{23}$$

where i_p is the incidence angle relative to the oncoming airflow (see Fig. 14) and a is the speed of sound. Improved modeling performance was obtained when M_{tip} was defined as a polynomial spline [50],

$$\left(M_{tip} - 0.3\right)_+ = \begin{cases} \left(M_{tip} - 0.3\right) & M_{tip} \geq 0.3 \\ 0 & M_{tip} < 0.3 \end{cases} \tag{24}$$

[§] Information available online at https://software.nasa.gov/software/ARC-16265-1 [accessed May 2021] which enacts the variable only when compressibility effects manifest. The candidate model terms consisted of expansions of each explanatory variable up to quartic terms as well as all arrangements of cross terms up to a total of fourth order. Reynolds number effects, which can be influential for subscale vehicles [51, 52], were deemed insignificant for the full-scale propulsors investigated in this work.

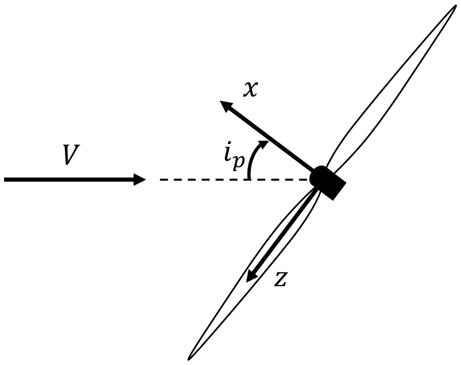

Fig. 14 Propulsor incidence angle definition and coordinate system.

An isolated pusher propeller model was developed using full-vehicle DOE CFD runs directly which were used previously to identify the full vehicle aero-propulsive model. This approach was taken, rather than using the BEMT simulation described above, because the pusher propeller effects can be more readily isolated between full-vehicle CFD data sets since it is a single variable; the approach also permits accounting for the vehicle presence effect on propeller performance. The data for propeller modeling was obtained using the difference between CFD data with the propeller-on (data previously used for transition and cruise flight regime model identification) and the full-vehicle model predictions with the propeller-off (the identified hover and glider models) to estimate the thrust and torque produced by the pusher propeller. These data were normalized by $\rho n^2 D^4$ and $\rho n^2 D^5$ to form the thrust coefficient and torque coefficient, respectively. Models for the propeller thrust and torque coefficient were then fit using a polynomial expansion of the normal component of advance ratio J_x as the regressors. Since the pusher propeller axis of rotation is oriented in the same direction as the body x-axis, J_x can be simply calculated as:

$$J_x = \frac{V \cos \alpha \cos \beta}{nD} = \frac{u}{nD} \tag{25}$$

The off-axis forces and moments for the pusher propeller were neglected, which is a reasonable assumption since the propeller generally operates at either low airspeed or low incidence angle. This approach resulted in a good model for the pusher propeller performance across the modeled flight envelope.

B. Aerodynamic Damping Predictions

All the above analysis concerns developing a static aero-propulsive model, however, dynamic aerodynamic effects have a significant influence on aircraft flight dynamics. Aerodynamic damping predictions are needed to add realism to eVTOL vehicle simulations, but present practical challenges to account for the isolated propulsors, bare airframe, and propulsion-airframe interaction aerodynamic damping contributions. For this work, low-fidelity damping predictions for the bare airframe and isolated propulsors were superimposed with the static aero-propulsive model to enable more realistic vehicle simulations, absent high-fidelity damping predictions. Damping associated with airframe-propulsion interaction effects were not considered, but it is recognized that these effects may have a significant effect on aerodynamic damping.

Bare airframe linear dynamic derivatives were estimated using a strip theory model of the aircraft [53]. Damping effects from isolated propulsors were estimated using the pusher propeller and rotor models discussed above. As described in detail in Ref. [15], relative velocity experienced by each propulsor is dependent on its location relative to the aircraft center of gravity, its orientation relative to the aircraft body-axes, the freestream velocity components u, v, w, and the vehicle body-axis angular velocity components, p, q, r. Consequently, nonzero vehicle angular velocity will change the force and moment production by each propulsor depending on its position and orientation on the vehicle. The propulsion damping aerodynamic forces and moments were estimated using the difference between the predicted forces and moments produced by each propulsor with and without vehicle angular velocity. In simulation, the propulsor forces and moments are then transformed to the body frame and added to the bare airframe aerodynamic damping predictions to augment the static aero-propulsive model with dynamic aerodynamic influences.

C. Flight Regime Synthesis

Although the four flight regime models (hover, transition, cruise, and glider) describe the Lift+Cruise aerodynamics over its operational flight envelope, the flight regimes are disjointed because different sets of propulsors are active in each model (see Tables 1-4). This results in a practical challenge of simulating a continuous vehicle flight mission where flying between multiple flight regimes is required. For example, it is required to fly between the hover and translation flight regimes as well as the transition and cruise flight regimes in a normal flight mission. For this work, the identified isolated propulsor models were used to obtain reasonable predictions of smooth movement between various flight regimes. Because it is not advised to extrapolate the vehicle aero-propulsive models outside the factor ranges used to identify each model, isolated propulsor models are used to make predictions outside of the propulsor range of validity for each flight regime model for use in a flight regime synthesis procedure. The force and moment predictions are then blended from the two flight modes being transitioned between.

As an example of the flight regime synthesis process, consider the movement between the transition (lifting rotors are active) and cruise flight regimes (lifting rotors are inactive), where there is a gap in modeled rotor speed between 0 to 550 RPM. For the cruise model, the predicted full-vehicle forces and moments assuming the rotors are not present (CM) are added to the predicted forces/moments from the isolated propulsion models for the current operating rotor speed ($PM(n_1, n_2, ..., n_8)$). In other words, this superimposes the cruise model with the isolated rotor forces and moments. For the transition model, the predicted full-vehicle forces and moments assuming the rotors are operating at their lower RPM limit ($TM(n_{1_L}, n_{2_L}, ..., n_{8_L})$) is added to the difference between predicted forces/moments from the isolated propulsion models at the current operating rotor speed ($PM(n_1, n_2, ..., n_8)$) and at the rotor speed set to the full-vehicle model boundary value ($PM(n_{1_L}, n_{2_L}, ..., n_{8_L})$). This effectively acts to remove rotor forces and moments from the transition model predictions. These pseudo-extrapolated transition and cruise model response predictions are then blended together using a quintic transition polynomial (see Ref. [15]), where the mean rotor speed value determines the weighting w_1 and w_2 given to the cruise and transition model predictions. This process to form a blended model (BM) prediction, in the form of an equation, is given as:

$$BM = w_1 \left[CM + PM(n_1, n_2, ..., n_8)\right] + w_2 \left[TM(n_{1_L}, n_{2_L}, ..., n_{8_L}) + PM(n_1, n_2, ..., n_8) - PM(n_{1_L}, n_{2_L}, ..., n_{8_L})\right]$$

Similar methods are used for movement between other flight regimes. Although propulsion-airframe interaction effects are not accurately captured for the propulsors used for blending, this methodology yields reasonable predictions and allows continuous simulation from hover through forward flight. It is also worth noting that a similar approach can be used to simulate propulsor failure scenarios.

D. Equations of Motion

Simulation of the Lift+Cruise aircraft was implemented using the kinematic and dynamic aircraft equations of motion developed under a standard set of assumptions [24, 54, 55]. The aircraft is modeled as a six degree-of-freedom rigid body treating the gyroscopic effects from the rotating portions of the propulsion system as applied external moments. The translational and rotational dynamics equations contain the forces X, Y, Z and moments L, M, N computed using the identified models, which include the collective contributions of propulsion and airframe effects as well as their interactions. The translational dynamics equations are,

$$\dot{u} = rv - qw - g\sin\theta + X/m \tag{26}$$

$$\dot{v} = pw - ru + g\cos\theta\sin\phi + Y/m \tag{27}$$

$$\dot{w} = qu - pv + g\cos\theta\cos\phi + Z/m \tag{28}$$

where, m is the aircraft mass, g is the gravitational acceleration, ϕ is the Euler roll angle, and θ is the Euler pitch angle, with all other variables following their earlier definition. The rotational dynamics equations augmented to include propulsor gyroscopic effects are,

$$I_x\dot{p} - I_{xz}\dot{r} = L + (I_y - I_z)qr + I_{xz}pq - (\dot{h}_x + qh_z - rh_y) \tag{29}$$

$$I_y\dot{q} = M + (I_z - I_x)pr + I_{xz}(r^2 - p^2) - (\dot{h}_y + rh_x - ph_z) \tag{30}$$

$$I_z\dot{r} - I_{xz}\dot{p} = N + (I_x - I_y)pq - I_{xz}qr - (\dot{h}_z + ph_y - qh_x) \tag{31}$$

where, I_x, I_y, I_z, I_{xz} are the aircraft moments of inertia and h_x, h_y, h_z are the net components of angular momentum of the propulsors, with all other variable definitions presented above. The angular momentum of a single propulsor about its axis of rotation is $h_p = I_p\Omega_p$, where I_p is the moment of inertia of the rotating portion of the propulsor and $\Omega_p = 2\pi n$ is the rotation rate in radians per second, with clockwise rotation as viewed from behind the propulsor being positive. For use in the above equations, the angular momentum for each propulsor about its axis of rotation is rotated into the aircraft body axes and then summed to compute the net angular momentum for all propulsors. If the rotors are operated symmetrically, their angular momentum components cancel, however, asymmetric rotor usage and the pusher propeller operation cause the propulsion gyroscopic effects to become significant.

E. Propulsion and Control Surface Actuator Dynamics

The aircraft equations of motion can be augmented with additional states to represent the dynamics associated with control surface actuation and propulsor speed changes. Lag associated with the propulsors are particularly important to consider for controller design, because propulsion dynamics can be significantly slower than control surface dynamics, particularly for full-scale eVTOL vehicles with fixed-pitch propulsors. A current open question for eVTOL vehicle design is if mechanically simpler rotational speed control is fast enough for vehicle stabilization at low speeds, or if more complex, higher-bandwidth variable-pitch control is necessary for reasonable controller performance. The propulsion dynamics are also directly affected by the propulsor moment of inertia and electrical motor characteristics. For this work, propulsor and control surface dynamics were modeled using first-order and second-order dynamics representing the lag between a commanded value and actual value. Expressed as a differential equation, these respectively take the form,

$$\dot{\delta} = \frac{1}{\tau}\left(\delta_{cmd} - \delta\right) \tag{32}$$

$$\ddot{\delta} + 2\zeta\omega_n\dot{\delta} + \omega_n^2\delta = \omega_n^2\delta_{cmd} \tag{33}$$

where δ is the actual value of a propulsor or control surface variable, δ_{cmd} is the corresponding commanded value, τ is first-order time constant, ω_n is the natural frequency, and ζ is the damping ratio. The dynamics equation order and constant parameters can be individually chosen and varied for each propulsor and control surface within the simulation.

IX. Conclusions

A novel computational approach for developing lift+cruise aircraft aero-propulsive models suitable for flight dynamics simulations has been presented. Models were developed and evaluated for the NASA Lift+Cruise concept aircraft's full operational envelope, which included four distinct modeled flight regimes: hover, transition, cruise, and glider. The modeling approach utilizing the RAM process was tailored specifically to lift+cruse vehicle attributes and specific flight regime characteristics. Models describing forward-flight aerodynamics reflected fixed-wing aircraft modeling techniques and models at low-speed conditions were similar to rotary-wing aircraft modeling techniques. Model identification challenges for computational experiments were described and practical mitigation strategies were discussed. Final models were shown to have good predictive capability and small normalized model fit error across the vehicle flight envelope. Additional eVTOL vehicle flight dynamics considerations necessary for accurate flight simulations were highlighted to inform future simulation activities. This work provides progress in eVTOL aircraft modeling research using computational techniques, but ongoing modeling studies are anticipated to further refine eVTOL vehicle aero-propulsive model development methodologies.

Acknowledgments

This research was funded by the NASA Aeronautics Research Mission Directorate (ARMD) Transformational Tools and Technologies (TTT) project and Revolutionary Vertical Lift Technologies (RVLT) project. Numerical simulations were performed using the NASA Advanced Supercomputing (NAS) System and the NASA Langley Research Center Mid-Range Computing Cluster. Vehicle flight dynamics simulation development support was provided by Thomas Britton. Constructive feedback from Irene Gregory, Jacob Cook, and Michael Acheson helped to guide the Lift+Cruise model development work described in this paper. Additional conversations with Eugene Morelli are acknowledged and appreciated.

Additional Tables

Table 6 Coefficient of determination, R^2, for each local model (expressed as a percentage)

Model Name	X or C_x	Y or C_y	Z or C_z	L or C_l	M or C_m	N or C_n
Hover Model ($-5 \leq u \leq +20$ kts)	96.6	96.8	98.8	99.1	99.1	97.7
Hover Model ($20 \leq u \leq 45$ kts)	93.4	96.2	99.0	99.3	99.0	97.3
Transition Model ($-5 \leq u \leq +7.5$ kts)	98.5	96.0	98.4	99.3	98.4	93.5
Transition Model ($7.5 \leq u \leq 20$ kts)	99.1	96.8	98.8	99.3	98.4	96.0
Transition Model ($20 \leq u \leq 45$ kts)	99.0	96.6	98.9	99.3	98.3	96.7
Transition Model ($45 \leq u \leq 70$ kts)	99.1	98.1	99.1	99.4	98.8	97.3
Transition Model ($70 \leq u \leq 95$ kts)	99.4	98.7	98.9	99.3	99.0	97.6
Cruise Model ($50 \leq u \leq 130$ kts)	99.9	99.3	99.9	99.9	99.6	99.4
Glider Model ($50 \leq u \leq 130$ kts)	99.6	99.3	99.9	99.9	99.3	99.2

Table 7 Number of model parameters identified for each local model

Model Name	X or C_x	Y or C_y	Z or C_z	L or C_l	M or C_m	N or C_n
Hover Model ($-5 \leq u \leq +20$ kts)	46	29	28	23	21	46
Hover Model ($20 \leq u \leq 45$ kts)	63	42	29	22	30	42
Transition Model ($-5 \leq u \leq +7.5$ kts)	15	39	24	24	32	71
Transition Model ($7.5 \leq u \leq 20$ kts)	21	39	27	29	36	52
Transition Model ($20 \leq u \leq 45$ kts)	24	48	35	26	37	55
Transition Model ($45 \leq u \leq 70$ kts)	30	40	27	23	36	52
Transition Model ($70 \leq u \leq 95$ kts)	28	32	24	29	40	39
Cruise Model ($50 \leq u \leq 130$ kts)	18	18	18	15	21	35
Glider Model ($50 \leq u \leq 130$ kts)	12	20	14	12	28	20

Table 8 Binomial analysis of residuals prediction error metric, e_{cv}^*, for each local model response (expressed as a percentage)

Model Name	X or C_x	Y or C_y	Z or C_z	L or C_l	M or C_m	N or C_n
Hover Model ($-5 \leq u \leq +20$ kts)	8.79	4.32	1.96	2.47	2.17	4.03
Hover Model ($20 \leq u \leq 45$ kts)	7.13	6.15	2.89	2.37	2.61	4.03
Transition Model ($-5 \leq u \leq +7.5$ kts)	4.72	6.69	2.88	2.22	3.31	7.51
Transition Model ($7.5 \leq u \leq 20$ kts)	6.25	4.35	3.04	2.36	2.87	3.79
Transition Model ($20 \leq u \leq 45$ kts)	5.37	5.49	2.40	2.00	2.73	5.19
Transition Model ($45 \leq u \leq 70$ kts)	4.23	3.58	2.25	1.90	2.36	3.84
Transition Model ($70 \leq u \leq 95$ kts)	3.26	3.28	1.98	2.30	2.36	4.45
Cruise Model ($50 \leq u \leq 130$ kts)	0.797	1.95	1.19	1.19	1.67	1.84
Glider Model ($50 \leq u \leq 130$ kts)	2.50	3.56	1.19	1.18	3.58	4.45

Table 9 Modeling data percent NRMSE for each local model response

Model Name	X or C_x	Y or C_y	Z or C_z	L or C_l	M or C_m	N or C_n
Hover Model ($-5 \leq u \leq +20$ kts)	3.48	2.62	1.77	1.50	1.46	2.36
Hover Model ($20 \leq u \leq 45$ kts)	4.08	3.28	1.64	1.32	1.44	2.41
Transition Model ($-5 \leq u \leq +7.5$ kts)	3.58	3.06	1.86	1.32	1.68	3.90
Transition Model ($7.5 \leq u \leq 20$ kts)	2.93	2.61	1.59	1.25	1.70	2.47
Transition Model ($20 \leq u \leq 45$ kts)	2.80	2.79	1.38	1.24	1.71	2.43
Transition Model ($45 \leq u \leq 70$ kts)	2.39	2.08	1.40	1.16	1.44	2.38
Transition Model ($70 \leq u \leq 95$ kts)	1.96	1.73	1.44	1.28	1.33	2.52
Cruise Model ($50 \leq u \leq 130$ kts)	0.509	1.08	0.689	0.687	0.937	1.03
Glider Model ($50 \leq u \leq 130$ kts)	1.70	1.74	0.693	0.711	1.92	2.07

Table 10 Validation data percent NRMSE for each local model response

Model Name	X or C_x	Y or C_y	Z or C_z	L or C_l	M or C_m	N or C_n
Hover Model ($-5 \leq u \leq +20$ kts)	5.23	3.04	1.38	1.53	1.47	2.82
Hover Model ($20 \leq u \leq 45$ kts)	4.64	3.98	1.69	1.52	1.61	2.69
Transition Model ($-5 \leq u \leq +7.5$ kts)	3.58	3.87	2.17	1.53	2.27	5.34
Transition Model ($7.5 \leq u \leq 20$ kts)	3.88	3.12	2.00	1.66	2.05	2.33
Transition Model ($20 \leq u \leq 45$ kts)	3.51	3.76	1.71	1.26	1.96	3.52
Transition Model ($45 \leq u \leq 70$ kts)	2.46	2.31	1.51	1.25	1.66	2.74
Transition Model ($70 \leq u \leq 95$ kts)	2.31	1.97	1.41	1.62	1.54	2.66
Cruise Model ($50 \leq u \leq 130$ kts)	0.478	1.17	0.768	0.766	0.966	1.12
Glider Model ($50 \leq u \leq 130$ kts)	1.87	2.07	0.688	0.733	2.04	2.53

References

[1] Johnson, W., Silva, C., and Solis, E., "Concept Vehicles for VTOL Air Taxi Operations," *AHS Technical Conference on Aeromechanics Design for Transformative Vertical Flight*, Jan. 2018.

[2] Silva, C., Johnson, W., Antcliff, K. R., and Patterson, M. D., "VTOL Urban Air Mobility Concept Vehicles for Technology Development," *2018 Aviation Technology, Integration, and Operations Conference*, AIAA Paper 2018-3847, Jun. 2018. https://doi.org/10.2514/6.2018-3847.

[3] Patterson, M. D., Antcliff, K. R., and Kohlman, L. W., "A Proposed Approach to Studying Urban Air Mobility Missions Including an Initial Exploration of Mission Requirements," *AHS International 74th Annual Forum & Technology Display*, May 2018.

[4] Antcliff, K. R., Whiteside, S. K. S., Kohlman, L. W., and Silva, C., "Baseline Assumptions and Future Research Areas for Urban Air Mobility Vehicles," *AIAA SciTech 2019 Forum*, AIAA Paper 2019-0528, Jan. 2019. https://doi.org/10.2514/6.2019-0528.

[5] Johnson, W., "NDARC — NASA Design and Analysis of Rotorcraft Theoretical Basis and Architecture," *American Helicopter Society Aeromechanics Specialists' Conference*, Jan. 2010.

[6] Fredericks, W., Antclif, K., Costa, G., Deshpande, N., Moore, M., San Miguel, E., and Snyder, A., "Aircraft Conceptual Design Using Vehicle Sketch Pad," *48th AIAA Aerospace Sciences Meeting Including the New Horizons Forum and Aerospace Exposition*, AIAA Paper 2010-658, Jan. 2010. https://doi.org/10.2514/6.2010-658.

[7] Saeed, A. S., Younes, A. B., Cai, C., and Cai, G., "A survey of hybrid Unmanned Aerial Vehicles," *Progress in Aerospace Sciences*, Vol. 98, 2018, pp. 91–105. https://doi.org/10.1016/j.paerosci.2018.03.007.

[8] Rothhaar, P. M., Murphy, P. C., Bacon, B. J., Gregory, I. M., Grauer, J. A., Busan, R. C., and Croom, M. A., "NASA Langley Distributed Propulsion VTOL Tilt-Wing Aircraft Testing, Modeling, Simulation, Control, and Flight Test Development," *14th AIAA Aviation Technology, Integration, and Operations Conference*, AIAA Paper 2014-2999, Jun. 2014. https://doi.org/10.2514/6.2014-2999.

[9] North, D. D., Busan, R. C., and Howland, G., "Design and Fabrication of the Langley Aerodrome No. 8 Distributed Electric Propulsion VTOL Testbed," *AIAA SciTech 2021 Forum*, AIAA Paper 2021-1188, Jan. 2021. https://doi.org/10.2514/6.2021-1188.

[10] Murphy, P. C., and Landman, D., "Experiment Design for Complex VTOL Aircraft with Distributed Propulsion and Tilt Wing," *AIAA Atmospheric Flight Mechanics Conference*, AIAA Paper 2015-0017, Jan. 2015. https://doi.org/10.2514/6.2015-0017.

[11] Busan, R. C., Rothhaar, P. M., Croom, M. A., Murphy, P. C., Grafton, S. B., and O'Neal, A. W., "Enabling Advanced Wind-Tunnel Research Methods Using the NASA Langley 12-Foot Low Speed Tunnel," *14th AIAA Aviation Technology, Integration, and Operations Conference*, AIAA Paper 2014-3000, Jun. 2014. https://doi.org/10.2514/6.2014-3000.

[12] Busan, R. C., Murphy, P. C., Hatke, D. B., and Simmons, B. M., "Wind Tunnel Testing Techniques for a Tandem Tilt-Wing, Distributed Electric Propulsion VTOL Aircraft," *AIAA SciTech 2021 Forum*, AIAA Paper 2021-1189, Jan. 2021. https://doi.org/10.2514/6.2021-1189.

[13] Simmons, B. M., and Murphy, P. C., "Wind Tunnel-Based Aerodynamic Model Identification for a Tilt-Wing, Distributed Electric Propulsion Aircraft," *AIAA SciTech 2021 Forum*, AIAA Paper 2021-1298, Jan. 2021. https://doi.org/10.2514/6.2021-1298.

[14] Simmons, B. M., and Hatke, D. B., "Investigation of High Incidence Angle Propeller Aerodynamics for Subscale eVTOL Aircraft," NASA TM–20210014010, May 2021.

[15] Simmons, B. M., "System Identification for Propellers at High Incidence Angles," *AIAA SciTech 2021 Forum*, AIAA Paper 2021-1190, Jan. 2021. https://doi.org/10.2514/6.2021-1190.

[16] Cooper, J. R., Ackerman, K. A., Rothhaar, P. M., and Gregory, I. M., "Autonomous Path-Following for a Tilt-Wing, Distributed Electric Propulsion, Vertical Take-Off and Landing Unmanned Aerial System in Hover Mode," NASA TM–2018–220109, Nov. 2018.

[17] Cook, J., and Gregory, I., "A Robust Uniform Control Approach for VTOL Aircraft," *VFS Autonomous VTOL Technical Meeting and Electric VTOL Symposium*, Jan. 2021.

[18] McSwain, R. G., Glaab, L. J., and Theodore, C. R., "Greased Lightning (GL-10) Performance Flight Research – Flight Data Report," NASA TM–2017-219794, Nov. 2017.

[19] Fredericks, W. J., McSwain, R. G., Beaton, B. F., Klassman, D. W., and Theodore, C. R., "Greased Lightning (GL-10) Flight Testing Campaign," NASA TM–2017-219643, Jul. 2017.

[20] Murphy, P. C., Hatke, D. B., Aubuchon, V. V., Weinstein, R., and Busan, R. C., "Preliminary Steps in Developing Rapid Aero Modeling Technology," *AIAA SciTech 2020 Forum*, AIAA Paper 2020-0764, Jan. 2020. https://doi.org/10.2514/6.2020-0764.

[21] Murphy, P. C., Simmons, B. M., Hatke, D. B., and Busan, R. C., "Rapid Aero Modeling for Urban Air Mobility Aircraft in Wind-Tunnel Tests," *AIAA SciTech 2021 Forum*, AIAA Paper 2021-1644, Jan. 2021. https://doi.org/10.2514/6.2021-1644.

[22] Murphy, P. C., Buning, P. G., and Simmons, B. M., "Rapid Aero Modeling for Urban Air Mobility Aircraft in Computational Experiments," *AIAA SciTech 2021 Forum*, AIAA Paper 2021-1002, Jan. 2021. https://doi.org/10.2514/6.2021-1002.

[23] Montgomery, D. C., *Design and Analysis of Experiments*, 8^{th} ed., John Wiley & Sons, Inc., Hoboken, NJ, 2013.

[24] Morelli, E. A., and Klein, V., *Aircraft System Identification: Theory and Practice*, 2^{nd} ed., Sunflyte Enterprises, Williamsburg, VA, 2016.

[25] Morelli, E. A., and Klein, V., "Application of System Identification to Aircraft at NASA Langley Research Center," *Journal of Aircraft*, Vol. 42, No. 1, 2005, pp. 12–25. https://doi.org/10.2514/1.3648.

[26] Hamel, P. G., and Jategaonkar, R. V., "Evolution of Flight Vehicle System Identification," *Journal of Aircraft*, Vol. 33, No. 1, 1996, pp. 9–28. https://doi.org/10.2514/3.46898.

[27] Tischler, M. B., and Remple, R. K., *Aircraft and Rotorcraft System Identification: Engineering Methods With Flight-Test Examples*, American Institute of Aeronautics and Astronautics, Reston, VA, 2006. https://doi.org/10.2514/4.861352.

[28] Hamel, P. G., and Kaletka, J., "Advances in Rotorcraft System Identification," *Progress in Aerospace Sciences*, Vol. 33, No. 3-4, 1997, pp. 259–284. https://doi.org/10.1016/S0376-0421(96)00005-X.

[29] Cunningham, M. A., and Hubbard, J. E., "Open-Loop Linear Model Identification of a Multirotor Vehicle with Active Feedback Control," *Journal of Aircraft*, Vol. 57, No. 6, 2020, pp. 1044–1061. https://doi.org/10.2514/1.C035834.

[30] Wei, W., Cohen, K., and Tischler, M. B., "System Identification and Controller Optimization of a Quadrotor UAV," *AHS 71st Annual Forum*, May 2015.

[31] Tobias, E. L., Sanders, F. C., and Tischler, M. B., "Full-Envelope Stitched Simulation Model of a Quadcopter Using STITCH," *AHS International 74th Annual Forum & Technology Display*, May 2018.

[32] Gong, A., Sanders, F. C., Hess, R. A., and Tischler, M. B., "System Identification and Full Flight-Envelope Model Stitching of a Package-Delivery Octocopter," *AIAA SciTech 2019 Forum*, AIAA Paper 2019-1076, Jan. 2019. https://doi.org/10.2514/6.2019-1076.

[33] Altamirano, G. V., and McCrink, M. H., "Investigation of Longitudinal Aero-Propulsive Interactions of a Small Quadrotor Unmanned Aircraft System," *AIAA SciTech 2021 Forum*, AIAA Paper 2021-1310, Jan. 2021. https://doi.org/10.2514/6.2021-1310.

[34] Landman, D., Simpson, J., Mariani, R., Ortiz, F., and Britcher, C., "Hybrid Design for Aircraft Wind-Tunnel Testing Using Response Surface Methodologies," *Journal of Aircraft*, Vol. 44, No. 4, 2007, pp. 1214–1221. https://doi.org/10.2514/1.25914.

[35] Klein, V., Batterson, J. G., and Murphy, P. C., "Determination of Airplane Model Structure from Flight Data by Using Modified Stepwise Regression," NASA TP-1916, Oct. 1981.

[36] Morelli, E. A., "Global Nonlinear Aerodynamic Modeling Using Multivariate Orthogonal Functions," *Journal of Aircraft*, Vol. 32, No. 2, 1995, pp. 270–277. https://doi.org/10.2514/3.46712.

[37] DeLoach, R., "Assessment of Response Surface Models Using Independent Confirmation Point Analysis," *48th AIAA Aerospace Sciences Meeting Including the New Horizons Forum and Aerospace Exposition*, AIAA Paper 2010-741, Jan. 2010. https://doi.org/10.2514/6.2010-741.

[38] Barron, A. R., "Predicted Squared Error: A Criterion for Automatic Model Selection," *Self-Organizing Methods in Modeling*, Farlow, S. J., Ed., Marcel Dekker, Inc., New York, NY, 1984, pp. 87–104.

[39] Derlaga, J. M., Jackson, C. W., and Buning, P. G., "Recent Progress in OVERFLOW Convergence Improvements," *AIAA SciTech 2020 Forum*, AIAA Paper 2020-1045, Jan. 2020. https://doi.org/10.2514/6.2020-1045.

[40] Buning, P. G., and Pulliam, T. H., "Near-Body Grid Adaption for Overset Grids," *46th AIAA Fluid Dynamics Conference*, AIAA Paper 2016-3326, Jun. 2016. https://doi.org/10.2514/6.2016-3326.

[41] Buning, P., Gomez, R., and Scallion, W., "CFD Approaches for Simulation of Wing-Body Stage Separation," *22nd Applied Aerodynamics Conference and Exhibit*, AIAA Paper 2004-4838, Aug. 2004. https://doi.org/10.2514/6.2004-4838.

[42] Ventura Diaz, P., and Yoon, S., "High-Fidelity Computational Aerodynamics of Multi-Rotor Unmanned Aerial Vehicles," *2018 AIAA Aerospace Sciences Meeting*, AIAA Paper 2018-1266, Jan. 2018. https://doi.org/10.2514/6.2018-1266.

[43] Jia, Z., and Lee, S., "Acoustic Analysis of a Quadrotor eVTOL Design via High-Fidelity Simulations," *25th AIAA/CEAS Aeroacoustics Conference*, AIAA Paper 2019-2631, May 2019. https://doi.org/10.2514/6.2019-2631.

[44] Chaffin, M. S., and Berry, J. D., "Helicopter Fuselage Aerodynamics Under a Rotor by Navier-Stokes Simulation," *Journal of the American Helicopter Society*, Vol. 42, No. 3, 1997, pp. 235–243. https://doi.org/10.4050/JAHS.42.235.

[45] Dommasch, D. O., *Elements of Propeller and Helicopter Aerodynamics*, Pitman Publishing Corporation, 1953.

[46] Gregory, I. M., Acheson, M. J., Bacon, B. J., Britton, T. C., Campbell, N. H., Cook, J. W., Holbrook, J. B., Moerder, D. D., Murphy, P. C., Neogi, N. A., Simmons, B. M., McMinn, J. D., and Buning, P. G., "Intelligent Contingency Management for Urban Air Mobility," *AIAA SciTech 2021 Forum*, AIAA Paper 2021-1000, Jan. 2021. https://doi.org/10.2514/6.2021-1000.

[47] Phillips, W. F., *Mechanics of Flight*, 2^{nd} ed., John Wiley & Sons, Hoboken, NJ, 2010.

[48] Johnson, W., *Rotorcraft Aeromechanics*, Cambridge University Press, 2013.

[49] Leishman, J. G., *Principles of Helicopter Aerodynamics*, 2^{nd} ed., Cambridge University Press, Cambridge, UK, 2016.

[50] Morelli, E. A., "Efficient Global Aerodynamic Modeling from Flight Data," *50th AIAA Aerospace Sciences Meeting including the New Horizons Forum and Aerospace Exposition*, AIAA Paper 2012-1050, Jan. 2012. https://doi.org/10.2514/6.2012-1050.

[51] Brandt, J., and Selig, M., "Propeller Performance Data at Low Reynolds Numbers," *49th AIAA Aerospace Sciences Meeting including the New Horizons Forum and Aerospace Exposition*, AIAA Paper 2011-1255, Jan. 2011. https://doi.org/10.2514/6.2011-1255.

[52] Deters, R. W., Ananda, G. K., and Selig, M. S., "Reynolds Number Effects on the Performance of Small-Scale Propellers," *32nd AIAA Applied Aerodynamics Conference*, AIAA Paper 2014-2151, Jun. 2014. https://doi.org/10.2514/6.2014-2151.

[53] Cook, J. W., and Hauser, J., "A Strip Theory Approach to Dynamic Modeling of Tiltwing eVTOL Aircraft," *AIAA SciTech 2021 Forum*, AIAA Paper 2021-1720, Jan. 2021. https://doi.org/10.2514/6.2021-1720.

[54] Etkin, B., and Reid, L. D., *Dynamics of Flight: Stability and Control*, 3^{rd} ed., John Wiley & Sons, Inc, New York, NY, 1996.

[55] Stevens, B. L., Lewis, F. L., and Johnson, E. N., *Aircraft Control and Simulation: Dynamics, Controls Design, and Autonomous Systems*, 3^{rd} ed., John Wiley & Sons, Hoboken, NJ, 2015.